

## **FORMULATION OF ANISOTROPIC MEDIUM IN SPATIAL NETWORK METHOD**

*N. Yoshida, S. Koike, N. Kukutsu, and T. Kashiwa*

- 1. Introduction**
  - 2. Spatial Network for 3-D Maxwell's Equation**
    - 2.1 Three-dimensional Spatial Network
    - 2.2 Bergeron's Expression of the 3-D Spatial Network
    - 2.3 Fundamental Treatment of Dispersive Medium
  - 3. Uniaxial Anisotropy**
    - 3.1 Treatment of Anisotropic Medium in the Spatial Network
    - 3.2 Analytical Results and Discussion
  - 4. Magnetized Ferrite**
    - 4.1 Formulation of Ferrite
    - 4.2 Nodal Equations and Equivalent Circuit
    - 4.3 Numerical Results and Discussion
  - 5. Magnetized Plasma**
    - 5.1 Treatment of Anisotropy in Equivalent Circuit
    - 5.2 Time-domain Formulation of Magnetized Cold Plasma by Trapezoidal Rule
    - 5.3 Bergeron's Formulation
    - 5.4 Numerical Results and Discussion
  - 6. Conclusion**
- References**

### **1. Introduction**

Recently, for many kinds of sphere of the engineering, a numerical analysis method has become much useful with the remarkable developments of the digital computer, especially the supercomputer. Also,

in the analyses of electromagnetic fields, the effectiveness of numerical analysis methods remarkably increases in solving problems with complex boundary and medium conditions. For example, the analysis of electromagnetic fields involving the anisotropic and dispersive medium has become more important in designing and estimating the characteristics of micro- and milli-meter wave devices and antennas. Furthermore, the digitalization, accompanied with the progress of ultra high speed pulse techniques, has increased the importance of the overall analyses of the system with respect to the time domain. Such analyses need to consider the direct relation between field variations at each time and spatial point, rather than formulation by the Helmholtz equation, such as the finite element method (FEM) and the boundary element method (BEM), supposing only a sinusoidal incident wave. In other words, by utilizing the direct vector formulation of the Maxwell's equation, the full-wave simulations of electromagnetic phenomena can be performed, especially in the three-dimensional analysis [1]. For this purpose, some finite difference methods such as the finite-difference time-domain method (FD-TD) and the transmission line matrix method (TLM) has been proposed, and are known to have many merits [2–8]. But to compute the time response, all the composed formula involving the medium characteristics should be formulated in the time domain. The above methods have some difficulties in the formulation of the characteristic equation of the dispersive and anisotropic medium in the time domain, which is caused by assigning a single field variable at each lattice point in space [9–10].

We have recently proposed a numerical vector analysis method, called as, the Spatial Network Method in three-dimensional space and the time domain [11–14]. This method is based on both the equivalent circuit of the Maxwell's equation and the formulation by the Bergeron's method in the time domain [15–17]. The structure of the three-dimensional equivalent circuit is fundamentally as same as that used in the FD-TD or the TLM methods, and the treatment of the line between each lattice node as the one-dimensional transmission line is identical to that of the TLM method. But in this method, the both voltage and currents variables are defined at each node in the equivalent circuit, and at each node, the continuity law of the current occurs. These treatment realizes the representation of the dispersive medium by the equivalent lumped-circuit elements at each node, and the difference formulation in the time domain is derived from the characteristic

differential equation of the medium by the trapezoidal rule. Also this treatment performs an iterative computation of the independent nodal equation at each node using only the values obtained at the previous time step. Moreover, the feature that two field variables for two different directions exist at each node is extended to the anisotropic medium by use of the equivalent mutual coupling between the field variables of the connected lines relating to the off-diagonal components in the permittivity or permeability tensor [18].

In this paper, as typical examples of the equivalent circuit and the Bergeron's formulation for a anisotropic medium with dispersive characteristics in the Spatial Network Method (SNM: referred here as the present method), we present fundamental formulation of the dielectric with uniaxial anisotropy and the gyro-anisotropic medium such as magnetized ferrite and the magnetized plasma. To show the validity of each formulation, some results are presented.

## 2. Spatial Network for 3-D Maxwell's Equation

### 2.1 Three-dimensional Spatial Network

In considering Maxwell's equation in a three-dimensional space, each field variable is assigned at each discrete point to satisfy the mutual relation between the variables derived from the equation. In Fig. 2.1, a three-dimensional lattice network model of Maxwell's equation is shown. Table 2.1 presents the correspondence of each component in Maxwell's equation to each of the respective points, which are identified in the figure as  $A$ ,  $B$ ,  $C$ ,  $D$ ,  $E$  and  $F$ . In the Spatial Network Method, an equivalent circuit is constructed on the following three principles; first, it is assumed that the interval between the discrete points is a one-dimensional line as same as that in the TLM method. Second, every point is treated as a node where the continuity law about electric or magnetic currents occurs; and finally, the medium conditions are expressed as lumped elements. The second formulation is made possible by defining the magnetic current by virtue of the duality which exists between the electric and magnetic fields.

For realization of the spatial network on these principles, all electromagnetic variables correspond to circuit variables at each node. As shown in Table 2.1, the equivalent voltage variables are given by  $V_u$  and  $V_u^*$ , and the equivalent current and equivalent magnetic current are given by  $I_u$  and  $I_u^*$  ( $u = x, y, z$ ), respectively. By using these equivalent circuit variables, each component in Maxwell's equation assigned at each node is transformed into a two-dimensional transmission equation. This equation expresses the transmission of the plane wave perpendicular to the direction of the equivalent voltage defined at each node. This property coincides with the connecting structure of the one-dimensional lines at each node. The usual node at which an electric field component is treated as a voltage variable is called an electric node and the dual node at which a magnetic field component is treated as a voltage variable is called a magnetic node. In the magnetic nodes, the correspondence of the circuit variables to the field variables has a duality to those in the electric nodes. That is, the two variables exchange their correspondences. The symbol '\*' represents the difference of correspondence at each kind of node. In these correspondences between the field variables and circuit variables, the polarity is decided by the direction of the electromagnetic field which constructs the Poynting vector. The Poynting vector has the same direction as the positive coordinate of each one-dimensional line. Therefore, the direction of the electric and magnetic currents coincides with that of the Poynting vector; that is, the direction of the energy flow. Thus, both currents have the same property as the real conduction current in the line. In the equivalent circuit, to match the duality of the circuit variables at both the electric and magnetic nodes, a gyrator (as shown in Fig. 2.2(b) (1) and (2)) is inserted in series with each magnetic node. As a result, in the one-dimensional transmission line, the usual correspondences of both the electric field to the voltage, and the magnetic field to the current, are realized. As a special case exists between nodes  $B$  and  $D$ , a negative gyrator is inserted. The above mentioned correspondence between the equivalent circuit variables and electromagnetic field variables, the gyrators and the Poynting vectors is expressed in the basic lattice network shown in Fig. 2.2(a), which is composed of each of the nodes used in the spatial network presented in Table 2.1.

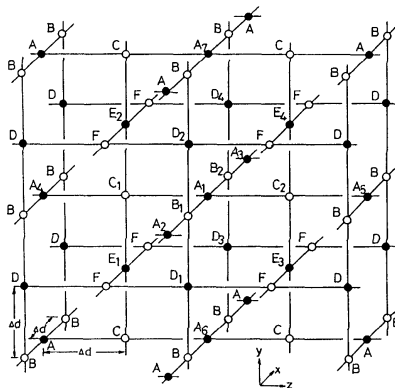
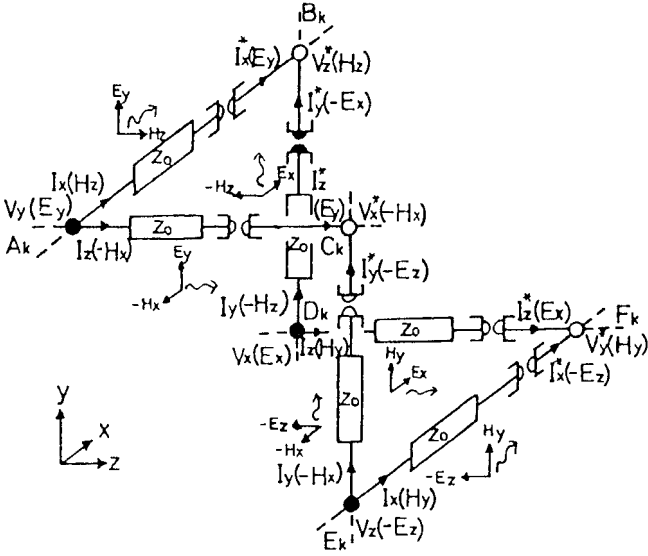


Figure 2.1 Three-dimensional lattice network. • Electric node, ○ Magnetic node, — One-dimensional transmission line.

Electric node			Magnetic node		
	Maxwell's equations	Variables		Maxwell's equations	Variables
A k	$\frac{\partial H_x}{\partial z} - \frac{\partial H_z}{\partial x} = \epsilon_0 \frac{\partial E_y}{\partial t}$	$V_y \equiv E_y$	F k	$\frac{\partial E_x}{\partial z} - \frac{\partial E_z}{\partial x} = -\mu_0 \frac{\partial H_y}{\partial t}$	$V_y^* \equiv H_y$
	$-\frac{\partial E_y}{\partial z} = -\mu_0 \frac{\partial H_x}{\partial t}$	$I_z \equiv -H_x$		$-\frac{\partial H_y}{\partial z} = \epsilon_0 \frac{\partial E_x}{\partial t}$	$I_z^* \equiv E_x$
	$\frac{\partial E_y}{\partial x} = -\mu_0 \frac{\partial H_z}{\partial t}$	$I_x \equiv H_z$		$\frac{\partial H_y}{\partial x} = \epsilon_0 \frac{\partial E_z}{\partial t}$	$I_x^* \equiv -E_z$
D k	$\frac{\partial H_z}{\partial y} - \frac{\partial H_y}{\partial z} = \epsilon_0 \frac{\partial E_x}{\partial t}$	$V_x \equiv E_x$	B k	$\frac{\partial E_y}{\partial x} - \frac{\partial E_x}{\partial y} = -\mu_0 \frac{\partial H_z}{\partial t}$	$V_z^* \equiv H_z$
	$\frac{\partial E_x}{\partial z} = -\mu_0 \frac{\partial H_y}{\partial t}$	$I_z \equiv H_y$		$\frac{\partial H_z}{\partial y} = \epsilon_0 \frac{\partial E_x}{\partial t}$	$I_y^* \equiv -E_x$
	$-\frac{\partial E_x}{\partial y} = -\mu_0 \frac{\partial H_z}{\partial t}$	$I_y \equiv -H_z$		$-\frac{\partial H_z}{\partial x} = \epsilon_0 \frac{\partial E_y}{\partial t}$	$I_x^* \equiv E_y$
E k	$\frac{\partial H_y}{\partial x} - \frac{\partial H_x}{\partial y} = \epsilon_0 \frac{\partial E_z}{\partial t}$	$V_z \equiv -E_z$	C k	$\frac{\partial E_z}{\partial y} - \frac{\partial E_y}{\partial z} = -\mu_0 \frac{\partial H_x}{\partial t}$	$V_x^* \equiv -H_x$
	$\frac{\partial E_z}{\partial y} = -\mu_0 \frac{\partial H_x}{\partial t}$	$I_y \equiv -H_x$		$\frac{\partial H_x}{\partial z} = \epsilon_0 \frac{\partial E_y}{\partial t}$	$I_z^* \equiv E_y$
	$-\frac{\partial E_z}{\partial x} = -\mu_0 \frac{\partial H_y}{\partial t}$	$I_x \equiv H_y$		$-\frac{\partial H_x}{\partial y} = \epsilon_0 \frac{\partial E_z}{\partial t}$	$I_y^* \equiv -E_z$
dielectric constant $C_0 = \epsilon_0 / 2$ permeability $L_0 = \mu_0 / 2$ polarization $\Delta C = \epsilon_0 \chi_e / 2 \cdot \Delta d$ conductivity $G = \sigma / 2 \cdot \Delta d$ magnetization $\Delta L = \mu_0 \chi_m / 2 \cdot \Delta d$			dielectric constant $L_0^* = \epsilon_0 / 2$ permeability $C_0^* = \mu_0 / 2$ magnetization $\Delta C^* = \mu_0 \chi_m / 2 \cdot \Delta d$ magnetic current loss $G^* = \sigma^* / 2 \cdot \Delta d$ polarization $\Delta L^* = \epsilon_0 \chi_e / 2 \cdot \Delta d$		

Table 2.1 Correspondence between the field variables in Maxwell's equation and the quantities at each kind of node in the equivalent circuit.



(a)



(b)

Figure 2.2 (a) Fundamental connection of the node in the network,  $\rightsquigarrow$  Direction of the Poynting vector. (b) Definition of gyrator in (a), (1) Positive gyrator, (2) Negative gyrator.

## 2.2 Bergeron's Expression of the 3-D Spatial Network

In the Bergeron method, the propagation characteristics in a one-dimensional line of a finite length are formulated in the time domain by using the voltages and currents at both ports of the line. The formulation is closely related to the d'Alembert solution, and the fundamental properties of wave fields formulated by the wave equation are iteratively computed along a characteristic line in the space and time domain, determined by the propagation velocity. By these principles, the formulation and the computation of the circuit equation involving the connected lumped elements can be realized at each discrete point. This is done by utilizing the two variables of voltage and current, and the independent relation of each discrete point at each given time by the existence of a propagation time.

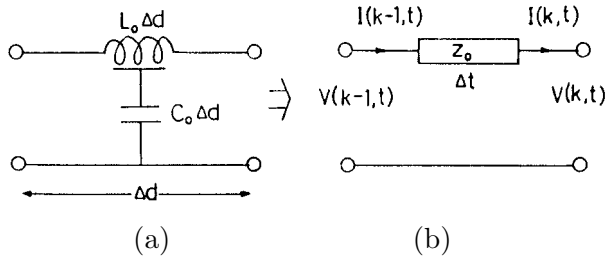


**Figure 2.3** A one-dimensional line (a) and its Bergeron expression (b).

In this section, a time-dependent expression of three-dimensional electromagnetic fields is derived by applying the Bergeron method to the three-dimensional spatial network (shown in section 2.1). In Fig. 2.3, Bergeron's expression for a one-dimensional transmission line is shown with a characteristic line impedance of  $z_0$  and a propagation time  $\Delta t$ ; thus,

$$z_0 = \sqrt{\frac{L_0}{C_0}} = \sqrt{\frac{\mu_0}{\epsilon_0}} = Z_0 \quad (1)$$

$$\Delta t = \Delta d \sqrt{L_0 C_0} = \Delta d \sqrt{\epsilon_0 \mu_0 / 2} = \Delta t_0 / \sqrt{2} \quad (2)$$

where  $L_0$  and  $C_0$  represent the inductance and the capacitance per unit length of the one-dimensional line in the three-dimensional spatial network given in Table 2.1.  $Z_0$  and  $\Delta t_0$  are the characteristic impedance and the propagation time of the plane wave in the free space, respectively.  $\Delta d$  is the length of the line and gives the interval

of the discretization in the three-dimensional spatial network. By supposing the parameter  $k$  as the number of discrete nodes, the following equations can be given for the forward and backward traveling waves.

$$V(k, t) + z_0 I(k, t) = V(k - 1, t - \Delta t) + z_0 I(k - 1, t - \Delta t) \quad (3a)$$

$$V(k - 1, t) - z_0 I(k - 1, t) = V(k, t - \Delta t) - z_0 I(k, t - \Delta t) \quad (3b)$$

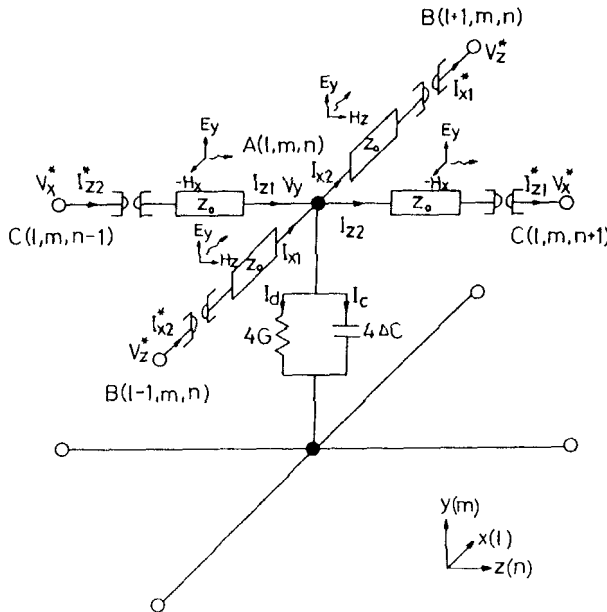


**Figure 2.4** Equivalent circuit at node  $A(l, m, n)$  including medium condition.

Here,  $V$  and  $I$  are the voltage and current at each discrete node. In Fig. 2.4, the equivalent circuit is shown at the electric node  $A$  where the electric field  $E_y$  is supposed to be a voltage variable. The spatial position in the directions  $x$ ,  $y$  and  $z$  is denoted by the discrete numbers  $l$ ,  $m$  and  $n$ , respectively. Time is expressed by  $t$ . In addition, in this figure, the one-dimensional lines between nodes are expressed temporarily as unbalanced lines. These are shown as solid lines in Fig. 2.1 for the sake of simplicity. In this circuit, the voltage between the lines corresponds to the electric field  $E_y$  and the values of the medium



conditions,  $\Delta C$  and  $G$ , correspond to the polarization and conductivity listed in Table 2.1. These values are quadruple those at each line because of the concentration of values at the node. Application of the Bergeron's equation, represented in equation (3), to each line connected to node  $A$  yields the following equations. These equations indicate the direction of the wave in relation to the node  $B$  and  $C$  by considering the series gyrators at the magnetic nodes.

$$V_y(l, m, n, t) + z_0 I_{z1}(l, m, n, t) = I_{z2}^*(l, m, n-1, t-\Delta t) + z_0 V_x^*(l, m, n-1, t-\Delta t) \quad (4a)$$

$$V_y(l, m, n, t) - z_0 I_{z2}(l, m, n, t) = I_{z1}^*(l, m, n+1, t-\Delta t) - z_0 V_x^*(l, m, n+1, t-\Delta t) \quad (4b)$$

$$V_y(l, m, n, t) + z_0 I_{x1}(l, m, n, t) = I_{x2}^*(l-1, m, n, t-\Delta t) + z_0 V_z^*(l-1, m, n, t-\Delta t) \quad (4c)$$

$$V_y(l, m, n, t) - z_0 I_{x2}(l, m, n, t) = I_{x1}^*(l+1, m, n, t-\Delta t) - z_0 V_z^*(l+1, m, n, t-\Delta t) \quad (4d)$$

Next, the lumped elements making up the medium condition can also be expressed by the Bergeron method. By defining the conductance current as  $I_d$ , the characteristics of the conductance  $G$  can be written as follows;

$$I_d(l, m, n, t) = 4G(l, m, n)V_y(l, m, n, t) \quad (5)$$

Also, the characteristics of the capacitance can be defined by using the trapezoidal expression of its characteristic equation, as follows;

$$V_y(l, m, n, t) - R_c(l, m, n)I_c(l, m, n, t) = V_y(l, m, n, t-\Delta t) + R_c(l, m, n)I_c(l, m, n, t-\Delta t) \quad (6a)$$

where

$$R_c(l, m, n) = \frac{\Delta t}{2[4\Delta C(l, m, n)]} \quad (6b)$$

Here,  $I_c$  and  $R_c$  respectively stand for the current through the capacitance and the characteristic resistance of the capacitance in the time domain. In the above equations, the expression of each parameter of the medium conditions as a function of the position shows the eligibility of applying the method to non-uniform fields by changing

the values of the parameters corresponding to the distribution of the medium. The right hand sides of equations (4) and (6a) are the already known values obtained from the voltage and current estimations, taken from the previous time step. By denoting each respective right hand side of the above equations as  $\Psi_1^*$ ,  $\Psi_2^*$ ,  $\Psi_3^*$ ,  $\Psi_4^*$ , and  $\Psi_c$ , and by using the following equation of the continuity of current at node A;

$$I_{z1} - I_{z2} + I_{x1} - I_{x2} - I_c - I_d = 0 \quad (7)$$

we can solve equations (4), (5) and (6a) according to the voltage  $V_y$ , yielding the next nodal equation at time  $t$ .

$$V_y(l, m, n, t) = \frac{R_c(l, m, n)(\Psi_1^* + \Psi_2^* + \Psi_3^* + \Psi_4^*) + z_0 \Psi_c}{z_0 + R_c(l, m, n) [4 + 4G(l, m, n)z_0]} \quad (8)$$

Each component of the current at time  $t$  is evaluated by substituting this  $V_y$  for that defined in each of equations (4), (5) and (6a), respectively. At other electric nodes, similar formulations can be performed. Also, at the magnetic nodes, by using the condition of the continuity of magnetic currents, a similar nodal equation can be derived thus;

$$V_u^*(l, m, n, t) = \frac{R_c^*(l, m, n)(\Psi_1 + \Psi_2 + \Psi_3 + \Psi_4) + z_0^* \Psi_c^*}{z_0^* + R_c^*(l, m, n) [4 + 4G^*(l, m, n)z_0^*]} \quad (9)$$

Here,  $z_0^* = z_0^{-1}$ , and  $\Delta C^*$  and  $G^*$  are the magnetic polarization and conductance listed in Table 2.1. Also,  $u$  corresponds to one of each  $(x, y, z)$  coordinate axis. In equations (8) and (9), every variable and parameter at a magnetic node is identified by the symbol  $*$ . These nodal equations formulated at every node are evaluated at time  $t$  from the previously obtained values. The values at the next time step are computed by using those obtained from the present. Thus, the time response of the field is iteratively evaluated.

### 2.3 Fundamental Treatment of Dispersive Medium

Consider the computation of the dispersive characteristics. By applying the trapezoidal approximation, a similar iterative calculation to the nodal equation can be performed. As an example, the orientation polarization can be thus treated since it has an important effect on

the property of the dielectric medium in the microwave band. The fundamental equation for the orientation polarization characteristics can be expressed by using the electric field  $E_u$  and polarization  $P_u$  in the direction  $u$  as follows.

$$\frac{dP_u(t)}{dt} + \frac{P_u(t)}{\tau} = \frac{\varepsilon_0 \chi_e}{\tau} E_u(t) \quad (10)$$

The term  $\tau$  is the relaxation time and  $\chi_e$  is the relative polarizability. Using the trapezoidal rule, the following difference form of the above equation is obtained.

$$P_u(t) - P_u(t - \Delta t) + \frac{P_u(t) + P_u(t - \Delta t)}{2\tau} \Delta t = \frac{\varepsilon_0 \chi_e [E_u(t) + E_u(t - \Delta t)]}{2\tau} \Delta t \quad (11)$$

Arranging this equation according to time  $t$  and  $t - \Delta t$  yields

$$\begin{aligned} \left(1 + \frac{\Delta t}{2\tau}\right) P_u(t) - \frac{\varepsilon_0 \chi_e \Delta t}{2\tau} E_u(t) = \\ \left(1 - \frac{\Delta t}{2\tau}\right) P_u(t - \Delta t) + \frac{\varepsilon_0 \chi_e \Delta t}{2\tau} E_u(t - \Delta t) \end{aligned} \quad (12)$$

The relation between the time variation of the polarization and the displacement current  $I_c$  is given as

$$I_c(t) = \frac{dP_u(t)}{dt} \quad (13)$$

Applying the trapezoidal approximation to the preceding equation yields

$$P_u(t) = \frac{I_c(t) + I_c(t - \Delta t)}{2} \Delta t + P_u(t - \Delta t) \quad (14)$$

$P_u(t)$  can be eliminated by substituting equation (14) for equation (12) to derive an equation with respect to  $E_u(t)$  and  $I_c(t)$ . Thus, eliminating  $P_u(t)$  and rewriting  $E_u$  as  $V_u$  yields the following equation of the orientation polarization approximated by the trapezoidal rule:

$$V_u(t) - R_p I_c(t) = -V_u(t - \Delta t) + R_p I_c(t - \Delta t) + V_p(t - \Delta t) \quad (15a)$$

$$R_p = \left( \frac{\tau}{\varepsilon_0 \chi_e} + \frac{\Delta t}{2\varepsilon_0 \chi_e} \right) \quad (15b)$$

$$V_p(t - \Delta t) = \frac{2P_u(t - \Delta t)}{\varepsilon_0 \chi_e} \quad (15c)$$

$R_p$  is the characteristic resistance of the polarization in the time domain and  $V_p(t - \Delta t)$  corresponds to the polarization of the previous time step. All the terms on the right hand side of equation (15a) are obtained from the previous time step. Thus, by supposing this right-hand side to be  $\Psi_c$  and rewriting  $R_p$  as  $R_c$ , the characteristics of the orientation polarization can be expressed in a form quite similar to that of the usual dielectric medium. It can also be computed iteratively by using equation (8) in the time domain. At each time ( $t$ ), the displacement current  $I_c(t)$  and the polarization  $P_u(t)$  are calculated by substituting the voltage  $V_u(t)$ , obtained from equation (8) for  $E_u(t)$  (in equations (15a) and (12)).

This treatment of the medium characteristics by the trapezoidal rule in the time domain can be further extended to the case of a non-magnetized plasma and resonance absorption. Also, for a ferrite and a magnetized plasma, a similar formulation by the trapezoidal rule can be applied by expressing their characteristic equations (including the bi-directional connections between the variables) as a mutually connected circuit.

### 3. Uniaxial Anisotropy

In this section, we treat the anisotropy of the dielectric constant caused by tilt of an optical axis. In the present method, the medium conditions are expressed by lumped elements at appropriate nodes. The off-diagonal elements in the permittivity tensor of the dielectric substrate demand the coupling of electric fields between different directions. The lumped circuit for those should be given at a node in which either of the coupled electric field components exists. Such a condition is satisfied at the magnetic node in which the electric fields correspond to the current variables. Therefore, given the duality of circuit variables, the diagonal and off-diagonal components of the dielectric constant are expressed by self-inductance and mutual inductance, respectively.

In the following sub-section, initially it is proved that the equivalent circuit with the mutual coupling represents anisotropy with off-diagonal elements in the permittivity tensor. Next, this treatment of the uniaxial anisotropy, with the permittivity tensor involving off-diagonal elements caused by tilt of an optical axis, is discussed in the case of the propagation characteristics for single and parallel strip lines on a dielectric substrate with tilted optical axis. Furthermore, to show the distinctive influence of anisotropy on the coupling property between lines, a parallel-line-type directional coupler on such a substrate is analyzed [19].

### 3.1 Treatment of Anisotropic Medium in the Spatial Network

In this section we prove that the equivalent circuit consisting of inductance with mutual coupling at magnetic nodes represents the electromagnetic wave equation in the anisotropic dielectric medium. We assume coupling between the dielectric fields  $E_y$  and  $E_x$ , use circuit variables as shown in Table 2.1. Figure 3.1 shows the arrangement of nodes around the  $A_1$  node in which the voltage variable  $V_y$  corresponds to the electric field  $E_y$ . Figure 3.2 shows details of nodes  $A$ ,  $B$ , and  $C$ . At the  $B$  nodes, lumped inductances involving mutual coupling give the property of anisotropic dielectric constants. Central difference equations are derived at all nodes  $B_1$ ,  $B_2$ , and  $C_1$ ,  $C_2$  that are adjacent to node  $A_1$  as follows;

$$V_y(A_2) - V_y(A_1) = 2\Delta x C_0^* \partial_t V_z^*(B_1) \quad (16a)$$

$$V_y(A_1) - V_y(A_3) = 2\Delta x C_0^* \partial_t V_z^*(B_2) \quad (16b)$$

$$- [V_x(D_1) - V_x(D_2)] = 2\Delta y C_0^* \partial_t V_z^*(B_1) \quad (16c)$$

$$- [V_x(D_3) - V_x(D_4)] = 2\Delta y C_0^* \partial_t V_z^*(B_2) \quad (16d)$$

$$V_y(A_4) - V_y(A_1) = 2\Delta z C_0^* \partial_t V_x^*(C_1) \quad (16e)$$

$$V_y(A_1) - V_y(A_5) = 2\Delta z C_0^* \partial_t V_x^*(C_2) \quad (16f)$$

$$V_z(E_1) - V_z(E_2) = 2\Delta y C_0^* \partial_t V_x^*(C_1) \quad (16g)$$

$$V_z(E_3) - V_z(E_4) = 2\Delta y C_0^* \partial_t V_x^*(C_2) \quad (16h)$$

where  $\Delta x$ ,  $\Delta y$ , and  $\Delta z$  are the lattice intervals in the  $x$ ,  $y$ , and  $z$  directions, respectively, and are equal to the constant value  $\Delta d$ .  $C_0^*$  corresponds to the free-space permeability  $\mu_0$  shown in Table 2.1, and  $\partial_t$  denotes  $\frac{\partial}{\partial t}$  for simplicity. In the following equations, for simplicity  $\partial_x$ ,  $\partial_y$ , and  $\partial_z$  also denote  $\frac{\partial}{\partial x}$ ,  $\frac{\partial}{\partial y}$ , and  $\frac{\partial}{\partial z}$ , respectively. Negative signed braces in (16c) and (16d) are derived from the opposite sign in the corresponding variables between the  $B$  and  $D$  nodes.

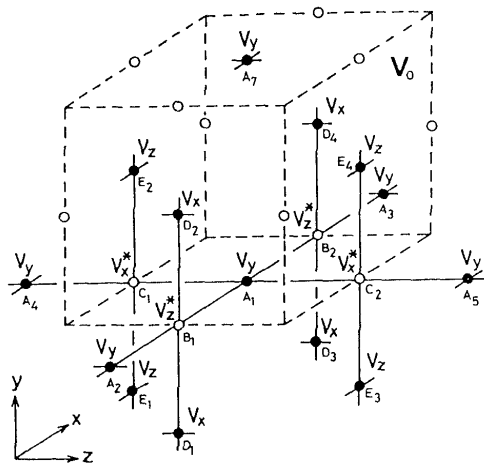


Figure 3.1 Arrangement of nodes around  $A_1$ .

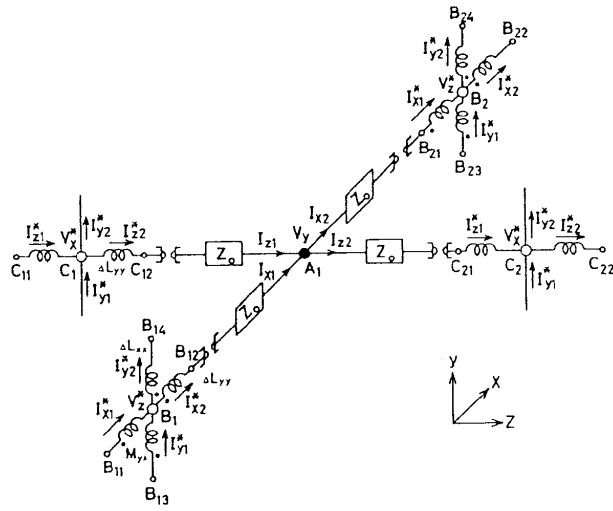


Figure 3.2 Details of nodes  $A$ ,  $B$ ,  $C$ .

Next, the voltages  $V_z^*$ ,  $V_x^*$  at  $B_1$ ,  $B_2$  and  $C_1$ ,  $C_2$  are expressed by current components  $I_{x1}$ ,  $I_{x2}$  and  $I_{z1}$ ,  $I_{z2}$  at  $A_1$ , as shown in Fig. 3.2. The voltage at  $B_1$  is expressed as follows by using  $\partial_x V_z^* = -L_0^* \partial_t I_x^*$ :

$$\begin{aligned} V_z^*(B_1) &= I_{x1}(A_1) - \Delta x \partial_x V_z^*(B_{12}) + \Delta V_z^*(B_{12}) \\ &= I_{x1}(A_1) + L_0^* \Delta x \partial_t I_{x2}^*(B_{12}) + \Delta L_{yy}^* \Delta z \partial_t I_{x2}^*(B_{12}) \\ &\quad + M_{yx}^* \Delta y \partial_t [-I_y^*(B_{13}) - I_y^*(B_{14})] \end{aligned} \quad (17a)$$

where  $\Delta V_z^*(B_{12})$  is the voltage drop at an inductance. At other nodes, the following relations are also formulated in the same manner.

$$\begin{aligned} V_z^*(B_2) &= I_{x2}(A_1) - L_0^* \Delta x \partial_t I_{x1}^*(B_{21}) - \Delta L_{yy}^* \Delta x \partial_t I_{x1}^*(B_{21}) \\ &\quad - M_{yx}^* \Delta y \partial_t [-I_y^*(B_{23}) - I_y^*(B_{24})] \end{aligned} \quad (17b)$$

$$V_x^*(C_1) = I_{z1}(A_1) + L_0^* \Delta z \partial_t I_{z2}^*(C_{12}) + \Delta L_{yy}^* \Delta z \partial_t I_{z2}^*(C_{12}) \quad (17c)$$

$$V_x^*(C_2) = I_{z2}(A_1) - L_0^* \Delta z \partial_t I_{z1}^*(C_{21}) - \Delta L_{yy}^* \Delta z \partial_t I_{z1}^*(C_{21}). \quad (17d)$$

Substituting (17) into (16) gives

$$\begin{aligned} V_y(A_2) - V_y(A_1) &= 2\Delta x C_0^* \partial_t I_{x1}(A_1) + 2\Delta x^2 C_0^* L_0^* \partial_t^2 I_{x2}^*(B_{12}) \\ &\quad + 2\Delta x^2 \Delta L_{yy}^* C_0^* \partial_t^2 I_{x2}^*(B_{12}) \\ &\quad + 2\Delta x \Delta y M_{yx}^* C_0^* \partial_t^2 [-I_y^*(B_{13}) - I_y^*(B_{14})] \end{aligned} \quad (18a)$$

$$\begin{aligned} V_y(A_1) - V_y(A_3) &= 2\Delta x C_0^* \partial_t I_{x2}(A_1) - 2\Delta x^2 C_0^* L_0^* \partial_t^2 I_{x1}^*(B_{21}) \\ &\quad - 2\Delta x^2 \Delta L_{yy}^* C_0^* \partial_t^2 I_{x1}^*(B_{21}) \\ &\quad - 2\Delta x \Delta y M_{yx}^* C_0^* \partial_t^2 [-I_y^*(B_{23}) - I_y^*(B_{24})] \end{aligned} \quad (18b)$$

$$\begin{aligned} -[V_x(D_1) - V_x(D_2)] &= 2\Delta y C_0^* \partial_t I_{x1}(A_1) \\ &\quad + 2\Delta y \Delta x C_0^* L_0^* \partial_t^2 I_{x2}^*(B_{12}) \\ &\quad + 2\Delta y \Delta x \Delta L_{yy}^* C_0^* \partial_t^2 I_{x2}^*(B_{12}) \\ &\quad + 2\Delta y^2 M_{yx}^* C_0^* \partial_t^2 [-I_y^*(B_{13}) - I_y^*(B_{14})] \end{aligned} \quad (18c)$$

$$\begin{aligned} -[V_x(D_3) - V_x(D_4)] &= 2\Delta y C_0^* \partial_t I_{x2}(A_1) - 2\Delta y \Delta x C_0^* L_0^* \partial_t^2 I_{x1}^*(B_{21}) \\ &\quad - 2\Delta y \Delta x \Delta L_{yy}^* C_0^* \partial_t^2 I_{x1}^*(B_{21}) \\ &\quad - 2\Delta y^2 M_{yx}^* C_0^* \partial_t^2 [-I_y^*(B_{23}) - I_y^*(B_{24})] \end{aligned} \quad (18d)$$

$$\begin{aligned}
V_y(A_4) - V_y(A_1) &= 2\Delta z C_0^* \partial_t I_{z1}(A_1) + 2\Delta z^2 C_0^* L_0^* \partial_t^2 I_{z2}^*(C_{12}) \\
&\quad + 2\Delta z^2 \Delta L_{yy}^* C_0^* \partial_t^2 I_{z2}^*(C_{12}) \quad (18e)
\end{aligned}$$

$$\begin{aligned}
V_y(A_1) - V_y(A_5) &= 2\Delta z C_0^* \partial_t I_{z2}(A_1) - 2\Delta z^2 C_0^* L_0^* \partial_t^2 I_{z1}^*(C_{21}) \\
&\quad - 2\Delta z^2 \Delta L_{yy}^* C_0^* \partial_t^2 I_{z1}^*(C_{21}) \quad (18f)
\end{aligned}$$

$$\begin{aligned}
V_z(E_1) - V_z(E_2) &= 2\Delta y C_0^* \partial_t I_{z1}(A_1) + 2\Delta y \Delta z C_0^* L_0^* \partial_t^2 I_{z2}^*(C_{12}) \\
&\quad + 2\Delta y \Delta z \Delta L_{yy}^* C_0^* \partial_t^2 I_{z2}^*(C_{12}) \quad (18g)
\end{aligned}$$

$$\begin{aligned}
V_z(E_3) - V_z(E_4) &= 2\Delta y C_0^* \partial_t I_{z2}(A_1) - 2\Delta y \Delta z C_0^* L_0^* \partial_t^2 I_{z1}^*(C_{21}) \\
&\quad - 2\Delta y \Delta z \Delta L_{yy}^* C_0^* \partial_t^2 I_{z1}^*(C_{21}) \quad (18h)
\end{aligned}$$

Assuming that  $\Delta x = \Delta y = \Delta z = \Delta d$ , to satisfy the continuity of currents  $I_{z1}$ ,  $I_{z2}$ ,  $I_{x1}$ , and  $I_{x2}$  at the  $A_1$  node, which are included in the first term of the right side of each equation in (18), the operation (18a)-(18b)+(18c)-(18d)+(18e)-(18f)+(18g)-(18h) is performed to give:

$$\begin{aligned}
&[V_y(A_2) + V_y(A_3) - 2V_y(A_1)] + [V_y(A_4) + V_y(A_5) - 2V_y(A_1)] \\
&\quad + [-V_x(D_1) + V_x(D_3) + V_z(E_1) - V_z(E_3)] \\
&\quad + [-V_x(D_4) + V_x(D_2) + V_z(E_4) - V_z(E_2)] \\
&= 4\Delta d C_0^* \partial_t [I_{x1} - I_{x2} + I_{z1} - I_{z2}]|_{A_1} \\
&\quad + 4\Delta d^2 C_0^* L_0^* \partial_t^2 [I_{x2}^*(B_{12}) + I_{x1}^*(B_{21}) \\
&\quad \quad + I_{z2}^*(C_{12}) + I_{z1}^*(C_{21})] \quad (19) \\
&\quad + 4\Delta d^2 \Delta L_{yy}^* C_0^* \partial_t^2 [I_{x2}^*(B_{12}) + I_{x1}^*(B_{21}) \\
&\quad \quad + I_{z2}^*(C_{12}) + I_{z1}^*(C_{21})] \\
&\quad + 4\Delta d^2 M_{yx}^* C_0^* \partial_t^2 [-I_y^*(B_{13}) - I_y^*(B_{14}) \\
&\quad \quad - I_y^*(B_{23}) - I_y^*(B_{24})]
\end{aligned}$$

The first term in the right hand side of (19) is eliminated by applying Kirchhoff's first law at the  $A_1$  node. Dividing both sides by  $4\Delta d^2$  and allowing  $\Delta d$  to approach zero, the left side converges to  $\nabla^2$  using the divergence theorem under a no-space-charge condition in volume  $V_0$  in Fig. 3.1:



$$\text{left side of (19)} = \nabla^2 V_y|_{A_1}. \quad (20a)$$

Also, the right side is transformed as follows:

$$\begin{aligned} & \text{right side of (19)} \\ &= 4C_0^* L_0^* \partial_t^2 \\ & \quad [I_{x2}^*(B_{12}) + I_{x1}^*(B_{21}) + I_{z2}^*(C_{12}) + I_{z1}^*(C_{21})] / 4 \\ &+ 4\Delta L_{yy}^* C_0^* \partial_t^2 \\ & \quad [I_{x2}^*(B_{12}) + I_{x1}^*(B_{21}) + I_{z2}^*(C_{12}) + I_{z1}^*(C_{21})] / 4 \\ &+ 4M_{yx}^* C_0^* \partial_t^2 \\ & \quad [-I_y^*(B_{13}) - I_y^*(B_{14}) - I_y^*(B_{23}) - I_y^*(B_{24})] / 4 \\ &= 4C_0^* (L_0^* + \Delta L_{yy}^*) \partial_t^2 \cdot \\ & \quad \left[ \frac{I_{x2}^*(B_{12}) + I_{x1}^*(B_{21}) + I_{z2}^*(C_{12}) + I_{z1}^*(C_{21})}{4} \right] \\ &+ 4C_0^* M_{yx}^* \partial_t^2 \cdot \\ & \quad \left[ \frac{-I_y^*(B_{13}) - I_y^*(B_{14}) - I_y^*(B_{23}) - I_y^*(B_{24})}{4} \right] \end{aligned} \quad (20b)$$

Here as  $\Delta d$  approaches zero all variables approach the values at the center node  $A_1$ .

$$\begin{aligned} (20b) &= 4C_0^* L^* \frac{\partial^2 V_y}{\partial t^2} \Big|_{A_1} \\ &+ 4C_0^* M_{yx}^* \cdot \frac{\partial^2 (-I_y^*)}{\partial t^2} \Big|_{\text{between } B_1 \text{ and } B_2, \text{ namely } A_1}. \end{aligned} \quad (21)$$

For generality we omit the position notation  $A_1$ . As a result, (20a) and (21) yield the wave equation

$$\nabla^2 V_y = 4C_0^* L^* \frac{\partial^2 V_y}{\partial t^2} + 4C_0^* M_{yx}^* \frac{\partial^2 (-I_y^*)}{\partial t^2} \quad (22)$$

From correspondence of variables,  $V_y|_A = E_y$ ,  $-I_y^*|_B = E_x$ ,  $L_0^* = \varepsilon_0/2$ ,  $C_0^* = \mu_0/2$ ,  $L^* = L_0^* + \Delta L_{yy}^* = \varepsilon_0(1 + \chi_{yy})/2 = \varepsilon_0\varepsilon_{yy}/2$ , and  $M_{yx}^* = \varepsilon_0\varepsilon_{yx}/2$  are derived. Therefore, (22) represents the following electromagnetic wave equation in the anisotropic medium:

$$\nabla^2 E_y = \varepsilon_0\varepsilon_{yy}\mu_0 \frac{\partial^2 E_y}{\partial t^2} + \varepsilon_0\varepsilon_{yx}\mu_0 \frac{\partial^2 E_x}{\partial t^2} \quad (23)$$

At other nodes in which the coupling between different field components occurs, the same formulations may be derived. We omit the description of Bergeron's formulation because the approximation of inductance and mutual coupling in the time domain by the trapezoidal rule is similar to that for capacitance.

### 3.2 Analytical Results and Discussion

The anisotropy used in this analysis is represented by the following dielectric tensor:

$$\varepsilon = \varepsilon_0 \begin{bmatrix} \varepsilon_\xi & 0 & 0 \\ 0 & \varepsilon_\eta & 0 \\ 0 & 0 & \varepsilon_z \end{bmatrix} \quad (24)$$

In (24),  $\varepsilon_\xi$  and  $\varepsilon_\eta$  are the principal optical axes of the relative dielectric constants of the substrate. The  $\xi\eta$  coordinate system may be tilted with respect to the  $xy$  coordinate system by angle  $\theta$ , as shown in Fig. 3.3. Using the coordinate transformation, the permittivity tensor in the  $xyz$  coordinate system is given by

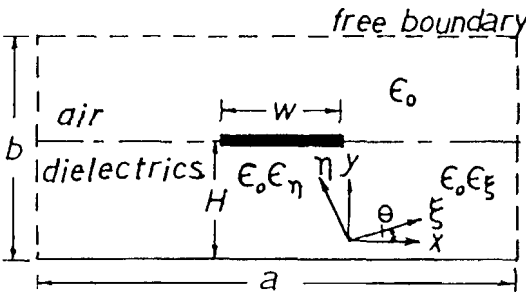
$$\varepsilon = \varepsilon_0 \begin{bmatrix} \varepsilon_{xx} & \varepsilon_{yx} & 0 \\ \varepsilon_{yx} & \varepsilon_{yy} & 0 \\ 0 & 0 & \varepsilon_z \end{bmatrix} \quad (25)$$

where

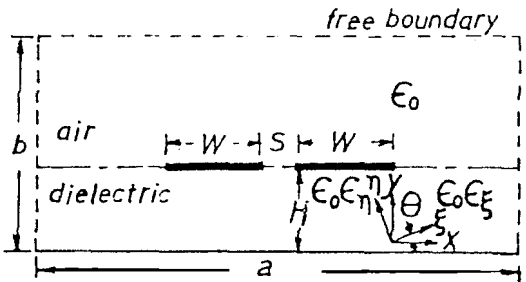
$$\varepsilon_{xx} = \varepsilon_\xi \cos^2 \theta + \varepsilon_\eta \sin^2 \theta \quad (26a)$$

$$\varepsilon_{yx} = (\varepsilon_\eta - \varepsilon_\xi) \sin \theta \cos \theta \quad (26b)$$

$$\varepsilon_{yy} = \varepsilon_\xi \sin^2 \theta + \varepsilon_\eta \cos^2 \theta \quad (26c)$$



(q)



(b)

Figure 3.3  $\xi\eta$  coordinate system tilted with respect to  $xy$  coordinate system by angle  $\theta$ , (a) Cross section of the microstrip line, (b) Cross section of parallel microstrip lines.

### 3.2.1 Characteristic Impedance and Effective Dielectric Constant

In order to verify the validity of the treatment of anisotropy in the present method, we calculated the characteristic impedance  $Z$  and effective dielectric constant  $\varepsilon_{eff}$  of a microstrip line and parallel strip lines on the anisotropic substrate as a function of tilt angles. The relationship between the tilted principal axes  $\varepsilon_\xi$ ,  $\varepsilon_\eta$  of dielectric constant and coordinate axes  $x$ ,  $y$  is shown in Fig. 3.3. Figure 3.3(a) and (b) shows the cross sections of microstrip line and parallel microstrip lines, respectively. The strip and ground conductors are assumed to have infinite conductivity. The dimensions of Fig. 3.3(a) are  $W/H = 0.5$ ,  $a/H = 10$ , and  $b/H = 3.5$ , and of Fig. 3.3(b) are  $W/H = 1.0$ ,  $S/H = 0.5$ ,  $a/H = 10$ , and  $b/H = 3.5$ . We consider sapphire as the anisotropic substrate, and assume that  $\varepsilon_\xi$ ,  $\varepsilon_\eta$ , and  $\varepsilon_z$  are 9.4, 11.6, and 9.4, respectively. In this analysis, the height of the substrate  $H = 4\Delta d$ , and one period of the applied sinusoidal wave is  $T = 213\Delta t$ , where  $\Delta t$  is the time interval between iterations. When  $1\Delta d$  is assumed to be 0.15mm, the frequency is  $f = 18.78$  GHz, and the height of the dielectric substrate becomes  $H = 0.6$  mm. If all space is filled with dielectric ( $\varepsilon_r = 11.6$ ), the wavelength becomes  $31.27\Delta d$ . It is generally known that the number of divisions of the period and the wavelength should be more than ten in the difference formulation. Therefore, the numbers of divisions for the period and wavelength in this analysis are sufficient for good resolution in time and space. In this condition, since the dimension of each part of the transmission line structure is very small compared with the guide wavelength  $\lambda_g$ , a quasi-static field condition giving TEM wave propagation may be assumed.

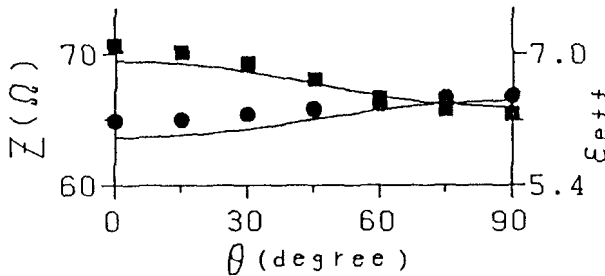


Figure 3.4 Characteristic impedance and effective dielectric constant of the microstrip line as a function of tilt angle.

The characteristic quantities are evaluated as follows in this analysis. The definition of characteristic impedance of microstrip is

$$Z = 2P_z/I_0^2 \quad (27)$$

and of two parallel strip lines is

$$Z = P_z/I_0^2 \quad (28)$$

where  $P_z$  is the time average of the Poynting vector propagating in the  $z$  direction, and  $I_0$  is the magnitude of the conduction current in one strip line. The Poynting vector propagating in the  $z$  direction is given by  $E_x \times H_y$  and  $E_y \times (-H_x)$ . Hence  $P$  is found by integrating these quantities in the  $xy$  cross section and by averaging the result over one period.  $I_0$  can be found by a line integral of the magnetic field along the integration path around the strip conductor. The effective dielectric constants may be found from the ratio of the free-space wavelength  $\lambda_0$  to the guide wavelength  $\lambda_g$ . Fig. 3.4 shows computed results of the impedance and effective dielectric constant of microstrip line as a function of tilt angle. The symbols  $\bullet$  and  $\blacksquare$  represent characteristic impedance and effective dielectric constant by the present method and the curves show analytical results [22]. In [22] the analyzed subject is shielded, but the position of the shielded is very far from the strip line, so our results, agree well with the analytical ones. The principal electric field of the propagating wave in the single strip line is  $E_y$ . When  $\theta = 0^\circ$  the  $\eta$  axis coincides with the  $y$  axis, so  $\varepsilon_{eff}$  is affected mainly by  $\varepsilon_\eta$ .  $\varepsilon_{eff}$  decreases and  $z$  increases as becomes more effective through an increase of  $\theta$  by rotating the anisotropic principal axis. Figure 3.5 shows computed results of the even- and odd-mode characteristic impedances  $Z_{oe}$  and  $Z_{oo}$  and the effective dielectric constants  $\varepsilon_{eff,even}$  and  $\varepsilon_{eff,odd}$  of parallel microstrip lines as a function of tilt angle. The symbol  $\bullet$  denotes the results by the present method, and the curves indicate the analytical results [22]. In the case of the even mode, the fundamental electric field of the propagating wave is  $E_y$ , so that  $\varepsilon_{eff,even}$  decreases and  $Z_{oe}$  increases with  $\theta$  increasing, as in the case of the single strip line shown in Fig. 3.4. On the other hand, for the case of the odd mode, between the strip lines there exists a notable x-directed component of the electric field in the propagating wave; hence the variation of  $Z_{oo}$  and  $\varepsilon_{eff,odd}$  with increasing  $\theta$  is not so evident as in the case of the even mode. But the variation of each

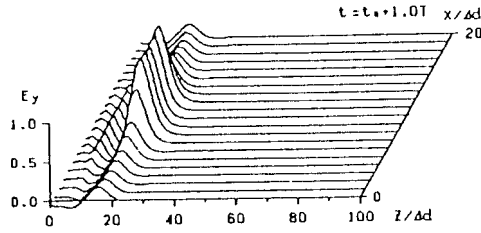
curve with  $\theta$  has the same tendency as that of the even mode. Thus the analytical curves and our results agree within a few percent, and the validity of treating anisotropy by the present method is confirmed.

**Figure 3.5** Even and odd mode characteristic impedance and effective dielectric constant of the parallel microstrip lines as a function of tilt angle.

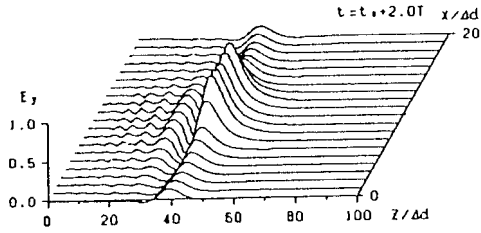
### *3.2.2 Time Dependence with $\theta$ Variation of Propagation of Pulse Waves*

To demonstrate the typical variation of propagation characteristics as a function of the tilt angle  $\theta$ , we present the time variation of the propagation of the pulse wave for single strip line. The values of the relative dielectric constants in the principal axes of the anisotropic substrate,  $\varepsilon_\xi$ ,  $\varepsilon_\eta$ , and  $\varepsilon_z$ , are chosen to be 1.75, 2.5, and 1.75, respectively. The large ratio of  $\varepsilon_\xi$  to  $\varepsilon_\eta$  gives a distinct change in the propagation velocity of the pulse wave. The pulse shape is a positive half-period of a sinusoidal wave having  $T = 71\Delta t$ . Figs. 3.6-3.8 clearly show an increasing tendency of propagation velocity with increasing tilt angle, in agreement with the physical reasoning described in the

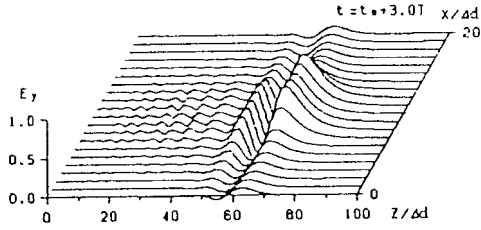
previous section. The variable  $t_o$  in the figures in an initial time at which the input wave is applied.



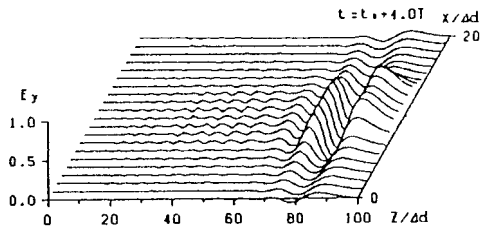
(a)



(b)



(c)



(d)

**Figure 3.6** Time variation of pulse wave in microstrip line at  $\theta = 0^\circ$  ( $\varepsilon_\xi = 1.75$ ,  $\varepsilon_\eta = 2.5$ ).

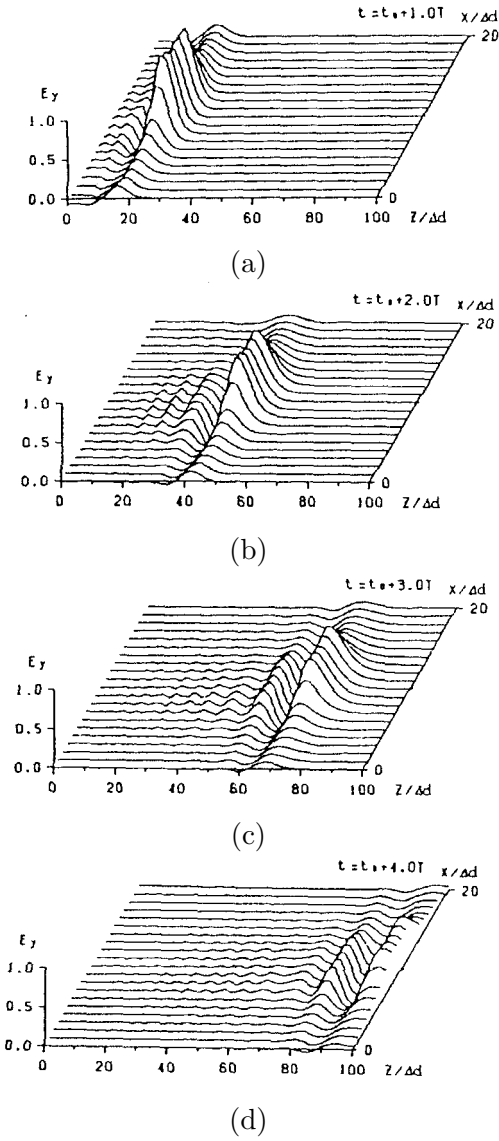
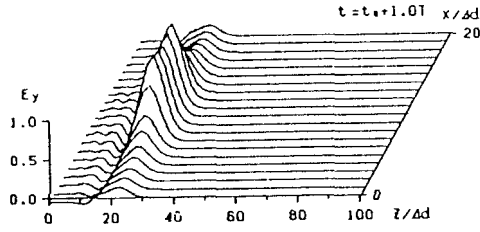
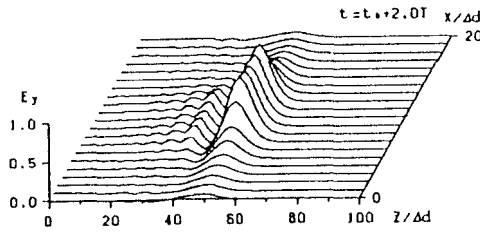


Figure 3.7 Time variation of pulse wave in microstrip line at  $\theta = 45^\circ$  ( $\varepsilon_\xi = 1.75$ ,  $\varepsilon_\eta = 2.5$ ).

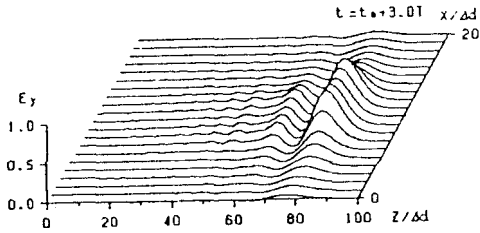




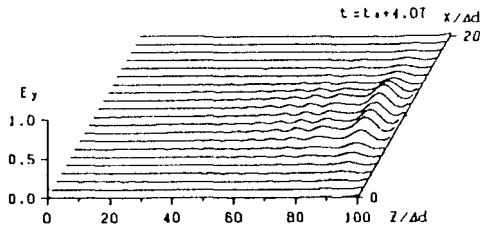
(a)



(b)



(c)



(d)

**Figure 3.8** Time variation of pulse wave in microstrip line at  $\theta = 90^\circ$  ( $\varepsilon_\xi = 1.75$ ,  $\varepsilon_\eta = 2.5$ ).

### 3.2.3 Characteristic of the Directional Coupler

In order to show the effect of anisotropy on the coupling between the lines, a parallel-line-type directional coupler is analyzed and its characteristics are presented as a function of the tilt angle of the anisotropic axis. Figure 3.9 shows the directional coupler. The dimensions in the  $x, y$ , and  $z$  directions of the analyzed region are  $40, 10$ , and  $100\Delta d$ , respectively. The strip and ground conductor are assumed to have infinite conductivity. There is an anisotropic substrate with thickness  $4\Delta d$  on the ground plane, and strip conductors with width  $6\Delta d$  as the directional coupler. The upper region is an air layer with thickness  $6\Delta d$ . The upper and side boundary of the analyzed region is approximated by a free boundary condition. The fundamental property of the directional coupler taken in this analysis is that an input at port 1 gives an output at port 2 and 4, and no output at port 3. The anisotropic substrate is assumed to be sapphire. The frequency of the input sinusoidal wave and the distance between ports 2 and 3 are adjusted to give maximum isolation for port 3 at  $\theta = 0^\circ$ . The period of the input wave is  $256\Delta t$  and " $\ell$ " in Fig. 3.9 is  $20\Delta d$ . Figures 3.10, 3.11, and 3.12 show the time variations of the spatial distribution, that is, the envelope of the maximum value at each point of the electric field  $E_y$  for  $\theta = 0^\circ, 45^\circ$ , and  $90^\circ$ , respectively. The expressions in the figures are the time intervals of a half-period used for finding the maximum value at each point to provide the spatial distribution rather than the instantaneous values. As the dimensions of each part of the coupler are very small compared with the guide wavelength, and the matching condition is realized at each port, the distributions seem to be corresponding to that for a pulse source. These figures look almost the same, but show the fine changes of the directional characteristic as a function of the tilt angle. Also, the time variation of each figure indicates the process by which the steady-state characteristics are obtained. The decrease of isolation is due to the decrease of  $\varepsilon_{eff}$  and the change of relative values between the  $Z_{oe}$  and  $Z_{oo}$ , as shown in Fig. 3.5.

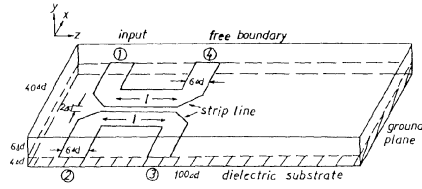
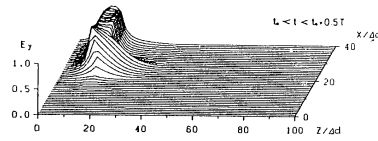
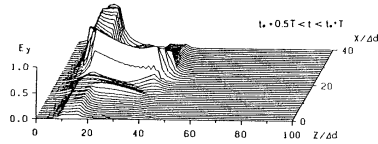


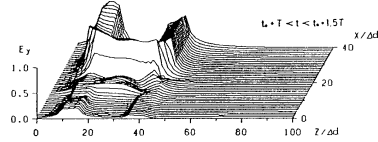
Figure 3.9 Parallel-line-type directional coupler ( $\varepsilon_\xi = 9.4$ ,  $\varepsilon_\eta = 11.4$  and  $\varepsilon_z = 9.4$ ).



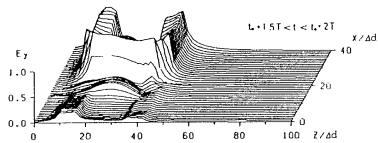
(a)



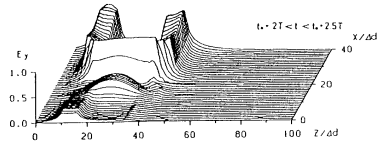
(b)



(c)

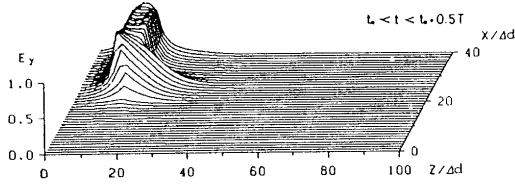


(d)

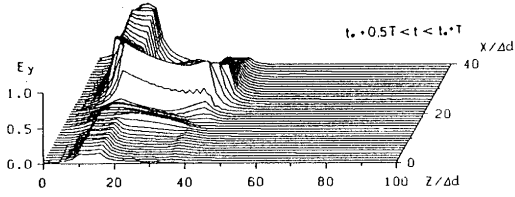


(e)

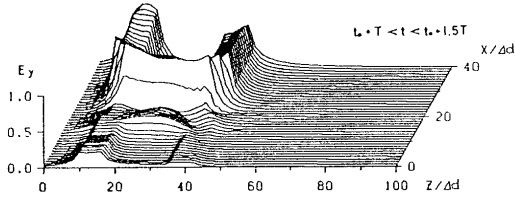
Figure 3.10 Time variation of spatial distribution of electric field  $E_y$  in the directional coupler at  $\theta = 0^\circ$ .



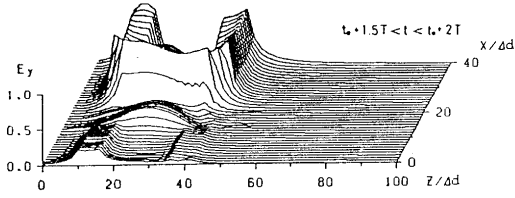
(a)



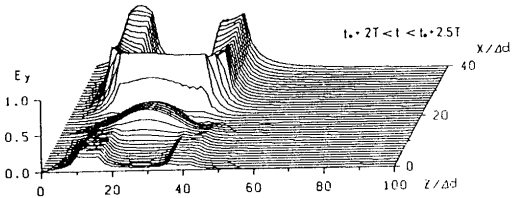
(b)



(c)

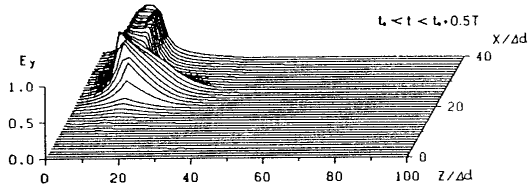


(d)

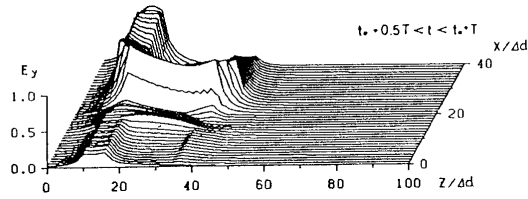


(e)

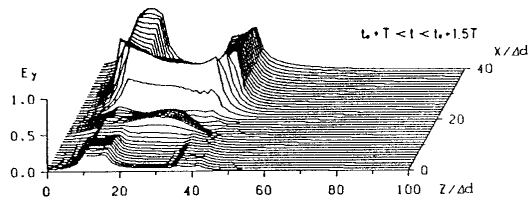
Figure 3.11 Time variation of spatial distribution of electric field  $E_y$  in the directional coupler at  $\theta = 45^\circ$ .



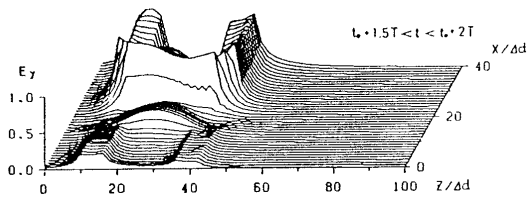
(a)



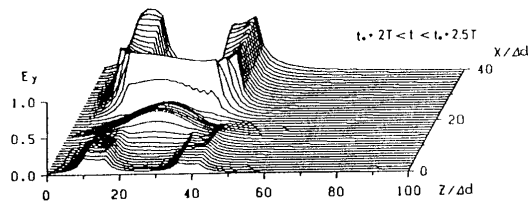
(b)



(c)



(d)



(e)

Figure 3.12 Time variation of spatial distribution of electric field  $E_y$  in the directional coupler at  $\theta = 90^\circ$ .

## 4. Magnetized Ferrite

The anisotropic medium has been applied to realized such nonreciprocal devices as gyrators, isolators, and circulators for the microwaves, millimeter-waves, and optical waves. In particular, for microwave and millimeter-wave circuits, ferrite is a typical gyro-anisotropic medium. The property of SNM, that in each node the current variables for two directions exist, also permits calculation of the effect of coupling between the magnetic fields, which is related to the off-diagonal elements of the permeability tensor [18]. In this section, the formulation of the magnetized ferrite in the three-dimensional space and time domain is presented. The characteristics of the formulation for the magnetized ferrite are summarized as follows.

1) An anisotropic medium is assumed with the lumped elements in each node in the equivalent circuit of Maxwell's equation. The tensor permeability of the ferrite is then expressed as the equivalent inductances with mutual coupling.

2) The characteristic differential equation of the magnetized ferrite is formulated as the difference equation in time domain by using the trapezoidal rule.

In the following sections, the formulation of the magnetized ferrite by the present method is described in detail. Next, in discussing the validity of the formulation, results are presented for two cases with respect to the relative angle between the directions of the DC magnetic field and wave propagation. One is for the wavelength versus DC magnetic field in perpendicularly magnetize rectangular waveguide; the other is for the characteristics of Faraday effect, such as the phase constant and rotated angle in the longitudinally magnetized cylindrical waveguide. For both cases, the results are discussed along with analytical ones, and the validity of the formulation is presented [20].

### 4.1 Formulation of Ferrite

Gilbert derived one differential form of phenomenological damping of ferrite that is often used. The equation of motion using the form of damping is written as

$$\frac{d\vec{M}}{dt} = -\gamma (\vec{M} \times \vec{H}) + \frac{\alpha}{M} \left( \vec{M} \times \frac{d\vec{M}}{dt} \right) \quad (29)$$

where  $\gamma$  is the gyromagnetic ratio ( $> 0$ ),  $M$  is the total magnetization,  $H$  is the total effective magnetic field, and  $\alpha$  is the loss parameter ( $> 0$ ).

Now, it is assumed that the direction of a DC magnetic field  $H_i$  and a saturated magnetization  $M_s$  are in the  $z$  direction; furthermore, an alternating magnetic field  $h$  and an RF magnetization  $m$  is assumed to be much smaller than  $H_i$  and  $M_s$ , respectively:

$$\vec{M} = \begin{bmatrix} m_x \\ m_y \\ M_s \end{bmatrix} \quad \vec{H} = \begin{bmatrix} h_x \\ h_y \\ H_i \end{bmatrix} \quad (30)$$

Expanding (29) with  $M$  and  $H$  in (30) leads to

$$\frac{dm_x}{dt} = -\gamma(-M_s h_y + H_i m_y) - \alpha \frac{dm_y}{dt} \quad (31a)$$

$$\frac{dm_y}{dt} = -\gamma(M_s h_x - H_i m_x) + \alpha \frac{dm_x}{dt} \quad (31b)$$

Rewriting the preceding equations yields

$$(1 + \alpha^2) \frac{d^2 m_x}{dt^2} + \omega_\tau \frac{dm_x}{dt} + \omega_i^2 m_x = \mu_0 \omega_i \omega_m h_x + \mu_0 \omega_{\alpha m} \frac{dh_x}{dt} + \mu_0 \omega_m \frac{dh_y}{dt} \quad (32a)$$

$$(1 + \alpha^2) \frac{d^2 m_y}{dt^2} + \omega_\tau \frac{dm_y}{dt} + \omega_i^2 m_y = \mu_0 \omega_i \omega_m h_y + \mu_0 \omega_{\alpha m} \frac{dh_y}{dt} - \mu_0 \omega_m \frac{dh_x}{dt} \quad (32b)$$

where

$$\omega_i = \gamma H_i \quad (32c)$$

$$\omega_m = \gamma M_s / \mu_0 \quad (32d)$$

$$\omega_\tau = 2\alpha \omega_i \quad (32e)$$

$$\omega_{\alpha m} = \alpha \omega_m \quad (32f)$$

The coupling between the variables of the different directions in the above equations is formulated as follows at the only node in which

both combined components exist. At node  $E$ , the magnetic field components  $H_x$  and  $H_y$ , and the electric field  $E_z$  are related from Table 2.1, so (32a) and (32b) can be used at node  $E$ , involving the coupling terms between  $H_x$  and  $H_y$ . And at node  $A$ , where  $H_x$ ,  $H_z$ , and  $E_y$  are concerned, the following equation, in which the coupling term is removed from (32a), is related by

$$(1 + \alpha^2) \frac{d^2 m_x}{dt^2} + \omega_\tau \frac{dm_x}{dt} + \omega_i^2 m_x = \mu_0 \omega_i \omega_m h_x + \mu_0 \omega_{\alpha m} \frac{dh_x}{dt} \quad (33)$$

This is also the case at node  $D$ , where  $H_y$ ,  $H_z$ , and  $E_x$  are concerned. So the following equation, in which the coupling term is removed from (32b), is related by

$$(1 + \alpha^2) \frac{d^2 m_y}{dt^2} + \omega_\tau \frac{dm_y}{dt} + \omega_i^2 m_y = \mu_0 \omega_i \omega_m h_y + \mu_0 \omega_{\alpha m} \frac{dh_y}{dt} \quad (34)$$

Thus, the equivalent circuit at every node in the ferrite is shown conceptually in Fig. 4.1, and a detailed conceptually equivalent circuit for node  $E$  is shown in Fig. 4.2. In this figure, the lumped inductance  $\Delta L_x$ ,  $\Delta L_y$  represent the noncoupling term in the equation, and the mutual coupling expression  $\Delta M_{xy}$  shows the coupling term. For the steady state, the former and the latter correspond to the diagonal elements and the off-diagonal elements of the permeability tensor, respectively.

The description is mainly of the formulation at node  $E$ , which is directly concerned with the gyroanisotropy of ferrite caused by the coupling term in the characteristic equation. Before the formulation of (32) by the trapezoidal rule, the electromagnetic variables are transformed to equivalent circuit ones. This treatment yields the formulation of the unified nodal equation by use of the continuity law of currents. At node  $E$ , the following correspondences are obtained from Table 2.1:

$$V_z = -E_z \quad (35a)$$

$$I_y = -H_x \quad (35b)$$

$$I_x = H_y. \quad (35c)$$

Furthermore, new equivalent circuit variables  $J_y$  and  $J_x$  are defined for magnetizations  $m_x$  and  $m_y$ , respectively. They obey the correspondences of the magnetic field, so the definitions are similar to those of (35b) and (35c), and are given by



$$J_y = -m_x \tag{36a}$$

$$J_x = m_y \tag{36b}$$

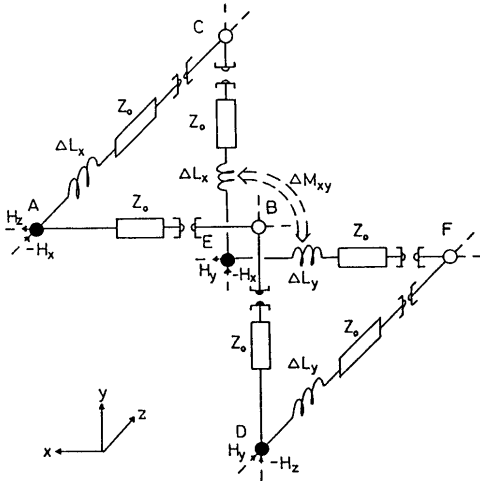


Figure 4.1 Unit equivalent circuit of magnetized ferrite for dc magnetic field  $H_z$ .

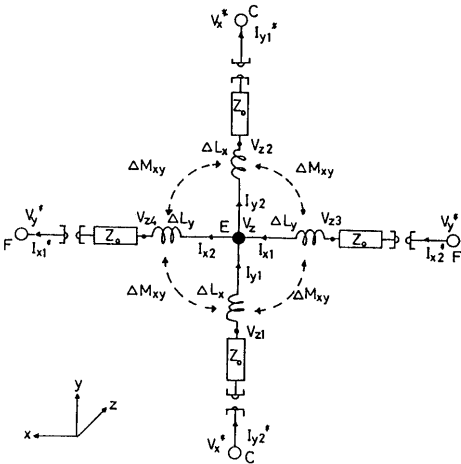


Figure 4.2 Equivalent circuit at node  $E(l, m, n)$  for DC magnetic field  $H_z$ .

At the electric node  $E$ , the magnetic field corresponds to the current variables in each connected line, so that  $J_y$  and  $J_x$  mean the magnetic flux of the equivalent inductance shown in Fig. 4.2. Using (35) and (36), (32a) and (32b) are rewritten as follows, respectively:

$$\frac{d^2 J_y}{dt^2} + k_\tau \frac{dJ_y}{dt} + k_i^2 J_y = k_{im} I_y + k_{\alpha m} \frac{dI_y}{dt} - k_m \frac{dI_x}{dt} \quad (37a)$$

$$\frac{d^2 J_x}{dt^2} + k_\tau \frac{dJ_x}{dt} + k_i^2 J_x = k_{im} I_x + k_{\alpha m} \frac{dI_x}{dt} + k_m \frac{dI_y}{dt} \quad (37b)$$

where

$$k_\tau = \omega_\tau / (1 + \alpha^2) \quad (37c)$$

$$k_i = \omega_i^2 / (1 + \alpha^2) \quad (37d)$$

$$k_{im} = \mu_0 \omega_i \omega_m / (1 + \alpha^2) \quad (37e)$$

$$k_{\alpha m} = \mu_0 \omega_{\alpha m} / (1 + \alpha^2) \quad (37f)$$

$$k_m = \mu_0 \omega_m / (1 + \alpha^2) \quad (37g)$$

These equations are the second differential equations with respect to time  $t$ , so they can be transformed to the difference form by twice using the trapezoidal rule.

By a first application of the trapezoidal rule to (37a) and (37b) at time  $t$ , we obtain

$$\begin{aligned} K_y(t) = & -\frac{k_i \Delta t}{2} (J_y(t) + J_y(t - \Delta t)) \\ & + \frac{k_{im} \Delta t}{2} (I_y(t) + I_y(t - \Delta t)) + K_y(t - \Delta t) \end{aligned} \quad (38a)$$

$$\begin{aligned} K_x(t) = & -\frac{k_i \Delta t}{2} (J_x(t) + J_x(t - \Delta t)) \\ & + \frac{k_{im} \Delta t}{2} (I_x(t) + I_x(t - \Delta t)) + K_x(t - \Delta t) \end{aligned} \quad (38b)$$

where

$$K_y(t) = \frac{dJ_y(t)}{dt} + k_\tau J_y(t) - k_{\alpha m} I_y(t) + k_m I_x(t) \quad (38c)$$

$$K_x(t) = \frac{dJ_x(t)}{dt} + k_\tau J_x(t) - k_{\alpha m} I_x(t) - k_m I_y(t) \quad (38d)$$

Here,  $\Delta t$  is the time difference. A second application of the trapezoidal rule to (38a) and (38b) at time  $t$ , using (38a) and (38b) at time  $t - \Delta t$ , yields

$$\begin{aligned}
 & \left(1 + k_\tau \frac{\Delta t}{2} + k_i \frac{\Delta t^2}{4}\right) J_y(t) - \left(k_{\alpha m} + k_{im} \frac{\Delta t}{2}\right) \frac{\Delta t}{2} I_y(t) \\
 & \quad + k_m \frac{\Delta t}{2} I_x(t) \\
 & = \left(1 - k_\tau \frac{\Delta t}{2} - k_i \frac{\Delta t^2}{4}\right) J_y(t - \Delta t) \\
 & \quad + \left(k_{\alpha m} + k_{im} \frac{\Delta t}{2}\right) \frac{\Delta t}{2} I_y(t - \Delta t) \\
 & \quad - k_m \frac{\Delta t}{2} I_x(t - \Delta t) + K_y(t - \Delta t) \Delta t
 \end{aligned} \tag{39a}$$

$$\begin{aligned}
 & \left(1 + k_\tau \frac{\Delta t}{2} + k_i \frac{\Delta t^2}{4}\right) J_x(t) - \left(k_{\alpha m} + k_{im} \frac{\Delta t}{2}\right) \frac{\Delta t}{2} I_x(t) \\
 & \quad - k_m \frac{\Delta t}{2} I_y(t) \\
 & = \left(1 - k_\tau \frac{\Delta t}{2} - k_i \frac{\Delta t^2}{4}\right) J_x(t - \Delta t) \\
 & \quad + \left(k_{\alpha m} + k_{im} \frac{\Delta t}{2}\right) \frac{\Delta t}{2} I_x(t - \Delta t) \\
 & \quad + k_m \frac{\Delta t}{2} I_y(t - \Delta t) + K_x(t - \Delta t) \Delta t
 \end{aligned} \tag{39b}$$

In this way, the second-order differential equations are changed to the first-order difference equations by definition of the variables  $K_y$  and  $K_x$ .

Next, in each connected line of the electric node, the time derivative of the flux  $J_y$ ,  $J_x$  causes the voltage drop  $V_y$ ,  $V_x$  in each inductance, respectively:

$$V_y(t) = \frac{dJ_y(t)}{dt} \tag{40a}$$

$$V_x(t) = \frac{dJ_x(t)}{dt} \tag{40b}$$

Equations (40a) and (40b) are also transformed to the difference form by using the trapezoidal rule:

$$J_y(t) = \frac{\Delta t}{2} (V_y(t) + V_y(t - \Delta t)) + J_y(t - \Delta t) \tag{41a}$$

$$J_x(t) = \frac{\Delta t}{2} (V_x(t) + V_x(t - \Delta t)) + J_x(t - \Delta t) \quad (41b)$$

Finally, substituting (41a) and (41b) into (39a) and (39b), respectively, the difference equations of voltage-current characteristics of the magnetized ferrite on time domain are as follows:

$$\begin{aligned} D_1 V_y(t) - D_2 I_y(t) + D_3 I_x(t) = & -D_1 V_y(t - \Delta t) + D_2 I_y(t - \Delta t) \\ & - D_3 I_x(t - \Delta t) - D_4 J_y(t - \Delta t) \\ & + D_5 K_y(t - \Delta t) \end{aligned} \quad (42a)$$

$$\begin{aligned} D_1 V_x(t) - D_2 I_x(t) - D_3 I_y(t) = & -D_1 V_x(t - \Delta t) + D_2 I_x(t - \Delta t) \\ & + D_3 I_y(t - \Delta t) - D_4 J_x(t - \Delta t) \\ & + D_5 K_x(t - \Delta t) \end{aligned} \quad (42b)$$

where

$$D_1 = \left( 1 + k_\tau \frac{\Delta t}{2} + k_i \frac{\Delta t^2}{4} \right) \frac{\Delta t}{2} \quad (42c)$$

$$D_2 = \left( k_{\alpha m} + k_{im} \frac{\Delta t}{2} \right) \frac{\Delta t}{2} \quad (42d)$$

$$D_3 = k_m \frac{\Delta t}{2} \quad (42e)$$

$$D_4 = k_\tau \Delta t + k_i \frac{\Delta t}{2} \quad (42f)$$

$$D_5 = \Delta t \quad (42g)$$

From equation (42), the inductance in Fig. 4.2 is defined as  $\Delta L_x = \Delta L_y = D_2/D_1$  and the conceptual mutual inductance  $\Delta M_{xy} = D_3/D_1$  is expressed by the arrow mark. In this expression, the gyroanisotropy is represented by the difference in sign between the third term on the left side of (42a) and (42b).

## 4.2 Nodal Equations and Equivalent Circuit

In Section 4.1, the equation of motion of ferrite is transformed to the difference equations using the equivalent variables relative to magnetization:  $J_x$ ,  $J_y$ , and  $K_x$ ,  $K_y$ . The definition of these variables makes it possible to complete the iterative computation on the time

domain by use of the values obtained only at the previous time step. In this section, these equations are combined with Bergeron's formulation of the one-dimensional line in the three-dimensional lattice networks shown in Fig. 2.1. The time difference at coincides with the transit time between two adjacent nodes in the lattice network. The connection of four lines is shown in Fig. 4. 2. As shown in the figure, by using the voltage variables  $V_{z1}$ ,  $V_{z2}$ ,  $V_{z3}$ , and  $V_{z4}$  in each line, the voltage drop of each inductance for (41a), (41b) is given by

$$V_{y1}(t) = V_{z1}(t) - V_z(t) \quad (43a)$$

$$V_{y2}(t) = V_z(t) - V_{z2}(t) \quad (43b)$$

$$V_{x1}(t) = V_{z3}(t) - V_z(t) \quad (43c)$$

$$V_{x2}(t) = V_z(t) - V_{z4}(t) \quad (43d)$$

where  $V_z(t)$  is the voltage of node  $E$ . It is assumed that the quantities of the variables of each coupling term in (42) are as follows. The current variable  $I_x$  in the  $x$  direction in (42a) is given by

$$I_x(t) = I_{x1}(t) + I_{x2}(t) \quad (44a)$$

Similarly, for  $I_y$  in the  $y$  direction in (42b),

$$I_y(t) = I_{y1}(t) + I_{y2}(t) \quad (44b)$$

Substituting (43a)-(43d) into (42a)-(42b) by considering (44a) and (44b), the difference equations for each inductance are as follows

$$\begin{aligned} & D_1 (V_{z1}(t) - V_z(t)) - D_2 I_{y1}(t) + D_3 I_x(t) \\ &= -D_1 V_{y1}(t - \Delta t) + D_2 I_{y1}(t - \Delta t) - D_3 I_x(t - \Delta t) \\ &\quad - D_4 J_{y1}(t - \Delta t) + D_5 K_{y1}(t - \Delta t) \end{aligned} \quad (45a)$$

$$\begin{aligned} & D_1 (V_z(t) - V_{z2}(t)) - D_2 I_{y2}(t) + D_3 I_x(t) \\ &= -D_1 V_{y2}(t - \Delta t) + D_2 I_{y2}(t - \Delta t) - D_3 I_x(t - \Delta t) \\ &\quad - D_4 J_{y2}(t - \Delta t) + D_5 K_{y2}(t - \Delta t) \end{aligned} \quad (45b)$$

$$\begin{aligned} & D_1 (V_{z3}(t) - V_z(t)) - D_2 I_{x1}(t) - D_3 I_y(t) \\ &= -D_1 V_{x1}(t - \Delta t) + D_2 I_{x1}(t - \Delta t) + D_3 I_y(t - \Delta t) \\ &\quad - D_4 J_{x1}(t - \Delta t) + D_5 K_{x1}(t - \Delta t) \end{aligned} \quad (45c)$$

$$\begin{aligned}
& TD_1(V_z(t) - V_{z4}(t)) - D_2I_{x2}(t) - D_3I_y(t) \\
& = -D_1V_{x2}(t - \Delta t) + D_2I_{x2}(t - \Delta t) + D_3I_y(t - \Delta t) \\
& \quad - D_4I_{x2}(t - \Delta t) + D_5K_{x2}(t - \Delta t)
\end{aligned} \tag{45d}$$

On the other hand, Bergeron's expression of each transmission line at node  $E(l, m, n)$  is given by

$$\begin{aligned}
V_{z1}(l, m, n, t) + z_0I_{y1}(l, m, n, t) = \\
I_{y2}^*(l, m - 1, n, t - \Delta t) + z_0V_x^*(l, m - 1, n, t - \Delta t)
\end{aligned} \tag{46a}$$

$$\begin{aligned}
V_{z2}(l, m, n, t) - z_0I_{y2}(l, m, n, t) = \\
I_{y1}^*(l, m + 1, n, t - \Delta t) - z_0V_x^*(l, m + 1, n, t - \Delta t)
\end{aligned} \tag{46b}$$

$$\begin{aligned}
V_{z3}(l, m, n, t) + z_0I_{x1}(l, m, n, t) = \\
I_{x2}^*(l - 1, m, n, t - \Delta t) + z_0V_y^*(l - 1, m, n, t - \Delta t)
\end{aligned} \tag{46c}$$

$$\begin{aligned}
V_{z4}(l, m, n, t) - z_0I_{x2}(l, m, n, t) = \\
I_{x1}^*(l + 1, m, n, t - \Delta t) - z_0V_y^*(l + 1, m, n, t - \Delta t)
\end{aligned} \tag{46d}$$

where the parameters  $l$ ,  $m$  and  $n$  denote the described position numbers in the  $x$ ,  $y$ , and  $z$  directions, respectively. And  $z_0$  is the characteristic impedance of the line at the electric node. Substituting (46a)-(46d) into (45a)-(45d) and eliminating  $V_{z1}$ ,  $V_{z2}$ ,  $V_{z3}$  and  $V_{z4}$ , the following equations were obtained. For simplicity, the position parameters  $l$ ,  $m$  and  $n$  are omitted in these equations:

$$D_1V_z(t) + (z_0D_1 + D_2)I_{y1}(t) - D_3I_x(t) = D_1A_1 - E_1 \tag{47a}$$

$$D_1V_z(t) - (z_0D_1 + D_2)I_{y2}(t) + D_3I_x(t) = D_1A_2 + E_2 \tag{47b}$$

$$D_1V_z(t) + (z_0D_1 + D_2)I_{x1}(t) + D_3I_y(t) = D_1A_3 - E_3 \tag{47c}$$

$$D_1V_z(t) - (z_0D_1 + D_2)I_{x2}(t) - D_3I_y(t) = D_1A_4 + E_4 \tag{47d}$$

where  $E_1 - E_4$  correspond to the right hand side of (45a)-(45d), and  $A_1 - A_4$  correspond to the right hand side of (46a)-(46d), respectively. These quantities are evaluated from values computed at a previous time step of the iterative procedure. By substituting, (47b) from (47a), and (47d) from (47c), the equation about  $I_x$  in (44a) and  $I_y$  in (44b) can be obtained, respectively. Whereas (47a)-(47d) become

$$D_1V_z(t) + (z_0D_1 + D_2)I_{y1}(t) = D_1A_1 - E_1 + D_3I_x(t) \tag{48a}$$

$$D_1 V_z(t) - (z_0 D_1 + D_2) I_{y2}(t) = D_1 A_2 + E_2 - D_3 I_x(t) \quad (48b)$$

$$D_1 V_z(t) + (z_0 D_1 + D_2) I_{x1}(t) = D_1 A_3 - E_3 - D_3 I_y(t) \quad (48c)$$

$$D_1 V_z(t) - (z_0 D_1 + D_2) I_{x2}(t) = D_1 A_4 + E_4 + D_3 I_y(t) \quad (48d)$$

The continuity of the current at node  $E(l, m, n)$  is given by

$$I_{y1}(t) - I_{y2}(t) + I_{x1}(t) - I_{x2}(t) = 0 \quad (49)$$

Substituting (48a)-(48d) into (49), the unified nodal equation at the time  $t$  is given by

$$V_z(l, m, n, t) = \frac{\Psi_1 + \Psi_2 + \Psi_3 + \Psi_4}{4D_1} \quad (50)$$

where  $\Psi_1$ ,  $\Psi_2$ ,  $\Psi_3$ , and  $\Psi_4$  correspond to the right side of (48a)-(48d), respectively. Each component of the currents at the time  $t$  is calculated by substituting  $V_z(t)$  in (49) into (48a)-(48d), respectively:

$$I_{y1}(t) = (\Psi_1 - D_1 V_z(t)) / (z_0 D_1 + D_2) \quad (51a)$$

$$I_{y2}(t) = -(\Psi_2 - D_1 V_z(t)) / (z_0 D_1 + D_2) \quad (51b)$$

$$I_{x1}(t) = (\Psi_3 - D_1 V_z(t)) / (z_0 D_1 + D_2) \quad (51c)$$

$$I_{x2}(t) = -(\Psi_4 - D_1 V_z(t)) / (z_0 D_1 + D_2) \quad (51d)$$

Similarly,  $V_{z1} - V_{z4}$  are computed by substituting (51a)-(51d) into (46a)-(46d). Also,  $J_{y1}$ ,  $J_{y2}$ ,  $J_{x1}$ , and  $J_{x2}$  are evaluated by substituting  $V_z(t)$  and  $V_{z1} - V_{z4}$  into (41a)-(41d) using (43a)-(43d), respectively. Finally,  $K_{y1}$ ,  $K_{y2}$ ,  $K_{x1}$ , and  $K_{x2}$  are obtained by substituting  $I_{y1}$ ,  $I_{y2}$ ,  $I_{x1}$ , and  $I_{x2}$ ,  $J_{y1}$ ,  $J_{y2}$ ,  $J_{x1}$ , and  $J_{x2}$  into (38a)-(38d). At each node  $E$ , the computation is performed, in this same procedure, for each time step. At node  $A$  and node  $D$ , the resultant formulations correspond to the noncoupling condition of that at node  $E$ . Then the time response of the field in the overall region is evaluated by the iterative procedure at each node, in the same manner similar to that at node  $E$ .

In this analysis, the direction of the DC magnetic field is supposed to the  $z$  direction, but for the case where the DC magnetic field is in the other direction, the equivalent circuit and the formulation are similarly brought about.

### 4.3 Numerical Results and Discussion

To examine the validity of the formulation described in the preceding section, two examples are taken with respect to the relative angles between the directions of the DC magnetic field and the wave propagation [23].

The first case is that where the angle is  $90^\circ$ . The characteristic of  $\lambda$  versus  $\sigma$  is computed for various  $\rho$ . Here,  $\lambda$  is the wavelength in the perpendicularly magnetized rectangular waveguide filled with the ferrite shown in Fig. 4.3. The length in the  $x$  direction is  $38\Delta d$ ; in the  $y$  direction it is  $148\Delta d$ , and in the  $z$  direction it is  $2\Delta d$ . The thin structure of the  $z$  direction yields only the propagation of the TE wave on the  $xy$  plane. Here  $\sigma$  is the ratio of the natural precession frequency to the signal frequency, and  $\rho$  is the ratio of the frequency associated with the saturation magnetization to the signal frequency. The wall of the waveguide is supposed to have infinite conductivity. The input of the sinusoidal wave is applied in each  $E$  node in the input  $DEF$  plane, which includes the  $D$ ,  $E$ , and  $F$  nodes shown in Fig. 2.1. The wavelength of the input wave  $\lambda_0$  is  $75\Delta d$  in free space. The mode of the input wave is assumed to be the TE mode. The output plane is terminated by the characteristic impedance of the  $TE_{10}$  mode to approximate the matching condition. Using this model, the results obtained are as shown in Fig. 4.4, where the dielectric constant  $\epsilon_r$  is fixed to be 2, and  $\sigma$  is changed under three parameters of  $\rho$ . The analytical curves of wavelength are calculated by using  $\mu_{eff}$ , which is determined from given  $\sigma$  and  $\rho$  by the following formula:

$$\lambda = \frac{\lambda_0 / \sqrt{\epsilon_r \mu_{eff}}}{\sqrt{1 - \left( \frac{\lambda_0}{\sqrt{\epsilon_r \mu_{eff}} \lambda_c} \right)^2}}$$

where

$$\mu_{eff} = \frac{\mu_r^2 - \kappa_r^2}{\mu_r}.$$

From the above description, the present method uses only primary parameters  $\sigma$  and  $\rho$  for the medium condition of ferrite. The good agreement in Fig. 4.4 of the computed wavelength with analytical ones shows the validity of the formulation. At steady state, the simulation presents the effect of  $\sigma$  and  $\rho$  as the effective permeability  $\mu_{eff}$ . The secondary parameters  $\mu_r$  and  $\kappa_r$  are also involved in the computation.



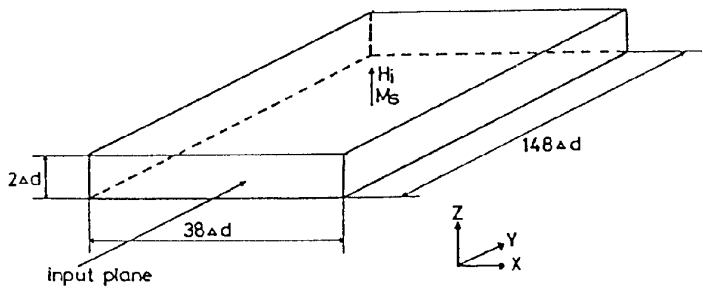


Figure 4.3 Analyzed model of rectangular waveguide filled with ferrite for DC magnetic field  $H_z$ .

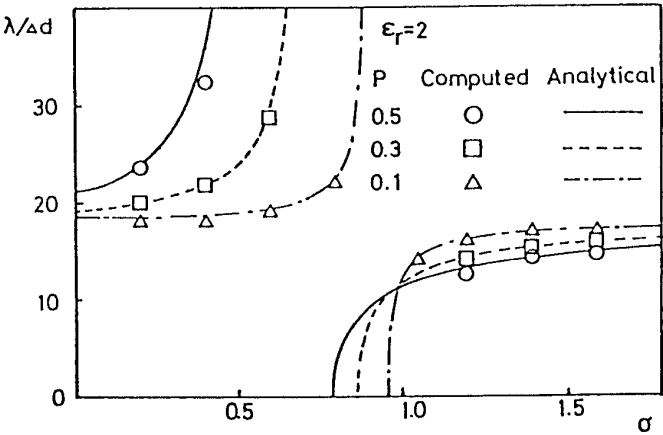
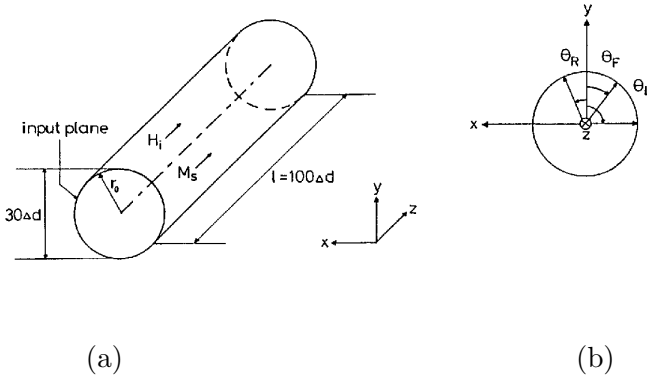


Figure 4.4 Characteristic of  $\lambda$  versus  $\sigma$  for various  $\rho$ , where  $\lambda$  is the wavelength,  $\sigma$  is the ratio of the natural precession frequency to the signal frequency, and  $\rho$  is the ratio of the frequency associated with the saturation magnetization to the signal frequency.

Next, the Faraday effect was simulated by a cylindrical waveguide containing ferrite. Figure 4.5(a) shows the analyzed model of the cylindrical waveguide. The direction of the dc magnetic field is the same longitudinal direction as the propagation. The radius of the waveguide is  $r_0 = 15d$ , and the longitudinal length in the  $z$  direction  $l = 100\Delta d$ . Figure 4.5(b) shows the coordinate system for the angle of the plane of the polarization  $\theta_L$ ,  $\theta_R$ , and  $\theta_F$  along the  $z$  direction for the L-wave, the R-wave, and the linear polarization, respectively. The boundary conditions of the wall also have perfect conductivity. The curve of the wall is approximated as stairs because of the cubical lattice network. For simplicity a detailed description of the treatment of these boundary conditions is not given. The input of the sinusoidal wave is applied in the input plane of  $ABD$ , and the mode of the input wave is assumed to be the  $TE_{11}$  mode. So the component  $E_y$  of the  $TE_{11}$  mode is applied at node  $A$  with correspondent amplitude distribution at the node. In similar fashion,  $E_x$  is also applied at node  $D_n$ . The R-wave and the L-wave are generated by shifting the phase of the  $E_x$  and  $E_y$  components of the input plane. The output plane is terminated by the characteristic impedance of the  $TE_{11}$  mode to appropriate the matching condition.



**Figure 4.5** (a) Analyzed model of cylindrical waveguide filled with ferrite with DC magnetic field  $H$ , (b) Coordinate system of angle of rotation  $\theta_L$  for L-wave,  $\theta_R$  for R-wave,  $\theta_F$  for linear polarization.

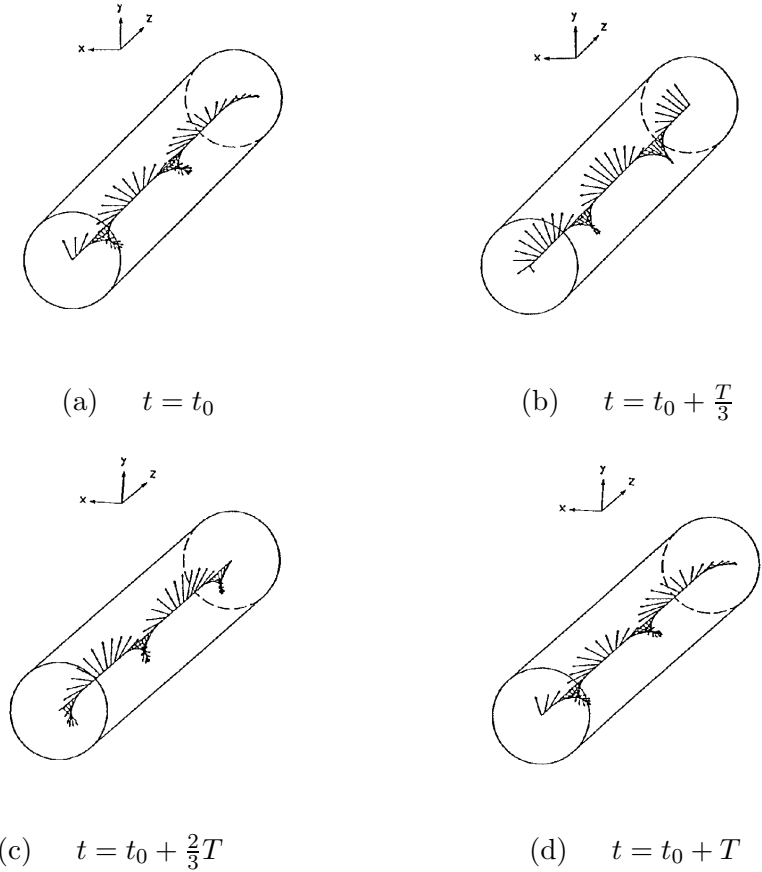
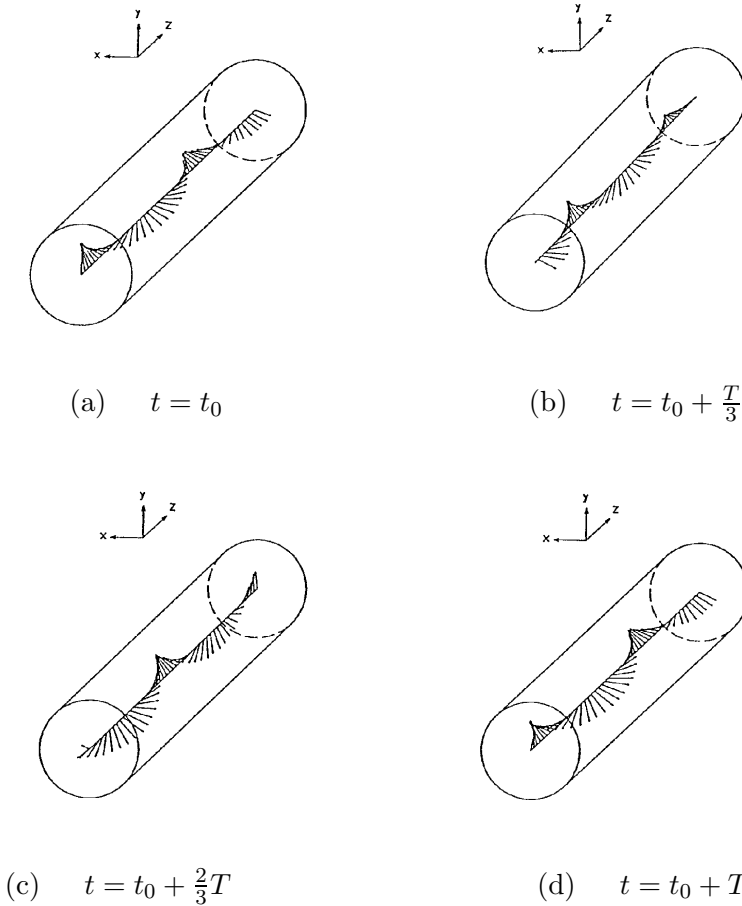


Figure 4.6 Time variation of electric field distribution of L-wave on central axis of waveguide ( $T$  is the period of an input wave.)



**Figure 4.7** Time variation of electric field distribution of R-wave on central axis of waveguide ( $T$  is the period of an input wave.)

Using this model, transient analysis is performed to show the process of Faraday rotation. In this case, the parameters of the ferrite are given by  $\theta$  ( $= \omega_i/\omega$ ) = 0.8,  $\rho$  ( $= \omega_m/\omega$ ) = 0.9, and  $\alpha = 0$ , which shows the period of the applied wave, is  $150\Delta t$ . This size of division, for the size of the cylindrical waveguide and the period of the applied sinusoidal wave, is sufficient for good resolution in space and time. The input is applied at  $t = 0$ .

Figures 4.6, 4.7, and 4.8 shows the instantaneous time variation of the rotation of the electric field for a period on the central axis for the input of the L-wave, the R-wave, and the linear polarization, respectively. As shown in Figs. 4.6 and 4.7, the electric field rotates to the left and the right, respectively, as the propagation distance in the  $z$  direction increases. In Fig. 4.8, the resultant rotation of linear polarization is observed, which is caused by the composition of the L-wave and the R-wave. These phenomena are supposed to be the effect of Faraday rotation. Theoretically, under conditions of actual use, the refractive index for the R-wave is smaller than that of the L-wave, so the phase velocity of R-wave is larger than that of the L-wave. Therefore,  $\theta_F$  should rotate to the right as the propagation distance in the  $z$  direction increases, as shown in Fig. 4.8. On the other hand, Fig. 4.9 shows the time variation of the instantaneous pattern of the electric field in the cross sections. In these figures, the rotation of the  $TE_{11}$  mode is shown. At each position on the  $z$  axis, the above condition causes the elliptical polarization that rotates to the right. Furthermore, to ascertain the realization of the Faraday rotation, there is an investigation into the composition of the L-wave and the R-wave of circular polarization that causes the rotation of the linear polarization. Figure 4.10 shows the variation of the angles  $\theta_L$  and  $\theta_R$  of the electric field of the L-wave and the R-wave versus the propagation distance along the  $z$  axis at  $t = t_0$ , as shown in Figs. 4.6 and 4.7, respectively. The angles  $\theta_L$  and  $\theta_R$  are in good proportion to the propagation distance, and the phase velocity of the L-wave is smaller than that of the R-wave. These results show that the propagation characteristics of the L-wave and the R-wave are well calculated. When comparing the time of  $(\theta_L - \theta_R)/2$  with plotted points  $\theta_F$ , they are in close agreement. For the Faraday rotation, the points of the maximum amplitude occur theoretically at the condition  $(\theta_L + \theta_R)/2 = 180n$  (where  $n$  is an integer). In this figure, this characteristic is also observed for each plotted points of  $\theta_F$ . Finally, there is an investigation into the phase constant in the parameters used. For these conditions, the analytically obtained value of the phase constant  $\beta/\beta_0$  of the L-wave and the R-wave are 1.696 and 1.291, respectively [23]. On the other hand, almost the same values are obtained in this analysis. So, by these considerations, it can be concluded that the Faraday effect of ferrite is simulated by this method.

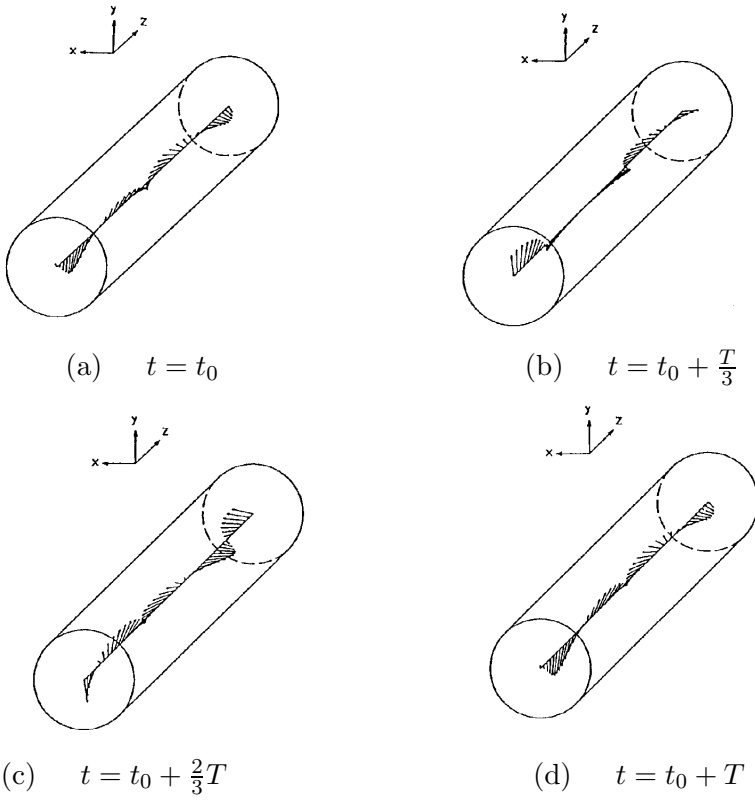


**Figure 4.8** Time variation of electric field distribution of linear polarization wave on central axis of waveguide ( $T$  is the period of an input wave.)

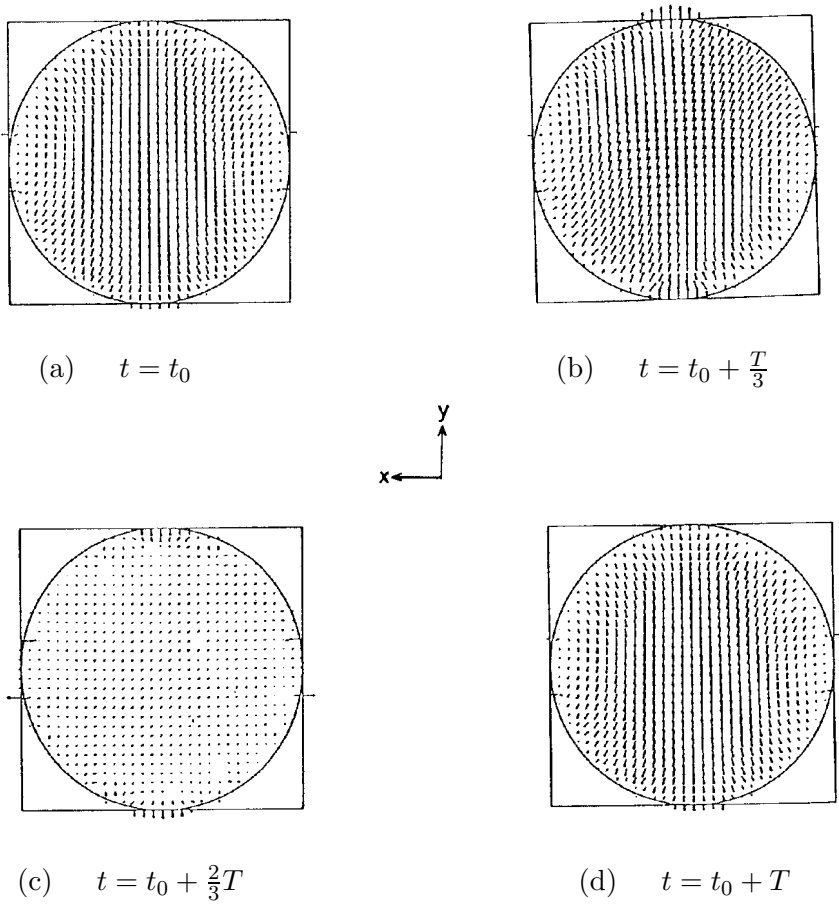


Figure 4.9 Time variation of electric field distribution of linear polarization wave on cross section ( $T$  is the period of an input wave.)

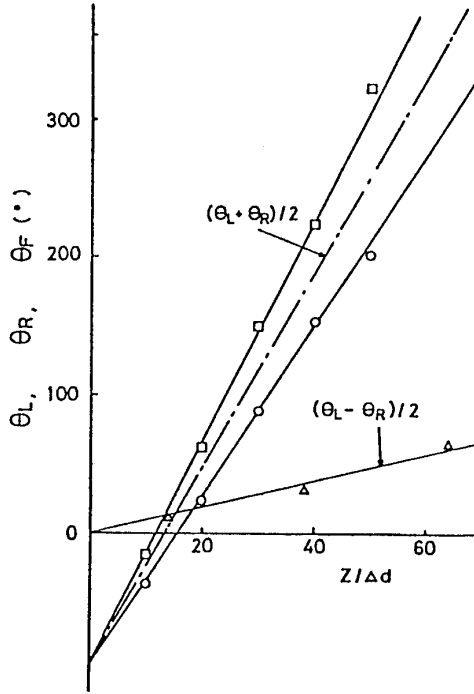


Figure 4.10 Angle of rotation  $\theta_L$ ,  $\theta_R$ , and  $\theta_F$  versus propagation distance.

## 5. Magnetized Plasma

The magnetized plasma has been studied in the context of the propagation of electromagnetic wave in the ionosphere. Now the study about the magnetized plasma has been widely extended with the development of new technologies, such as satellite communications, nuclear fission, and solid-state plasmas. But, because of its gyroelectric anisotropy and dispersion characteristics, the analysis is complicated, and three-dimensional treatment is indispensable. Therefore, for these studies the unified time-domain formulation of both the characteristics of the medium and the boundary conditions is necessary to cal-



culate exactly total field response. However, the formulation and its computation by analytical methods involving all these conditions are usually very complicated and difficult. Therefore, numerical analysis is required.

If a simulation is to faithfully reflect the mechanism or process of a natural phenomenon, such as anisotropy or dispersion, the formulation should be composed of basic equations which describe the mechanisms of the phenomenon. For magnetized plasma the motion of charged particles in the magnetized plasma is used.

As the present method assigns dual field variables at each node, the coupling between the field components caused by the anisotropy must be accounted for at which the related field variables exist. This coupling between fields corresponds to off-diagonal elements of the tensor permittivity and can be modeled as mutual coupling or a dependent source at each node.

### 5.1 Treatment of Anisotropy in Equivalent Circuit

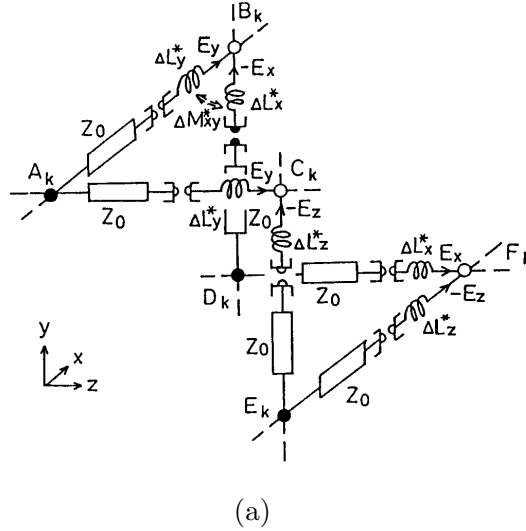
For an anisotropic medium, such as a cold plasma magnetized in the  $z$  directions, permittivity  $\vec{\epsilon}_r$  is given as follows:

$$\vec{\epsilon}_r = \begin{pmatrix} \epsilon_{xx} & \epsilon_{xy} & 0 \\ \epsilon_{yx} & \epsilon_{yy} & 0 \\ 0 & 0 & \epsilon_{zz} \end{pmatrix} = \begin{pmatrix} 1 + \chi_{xx} & \chi_{xy} & 0 \\ \chi_{yx} & 1 + \chi_{yy} & 0 \\ 0 & 0 & 1 + \chi_{zz} \end{pmatrix} \quad (52)$$

In this section, the time-domain formulation of the magnetized cold plasma in three-dimensional space by the spatial network method is described in detail. Then two principal problems are studied. First, for the transversely magnetized parallel-plate wave guide, the wavelength of the plane wave is computed and the agreement with analytical values is discussed. Next, for the longitudinally magnetized cylindrical waveguide, the characteristics of the Faraday rotation are simulated and discussed [21].

The conceptual equivalent circuit can be given by the model shown in Fig. 5.1 (a). Figure 5.1(b) shows correspondences between the tensor elements and the equivalent self- and mutual inductances where the  $\chi_{ij}$  are the polarizabilities in (52). The steady-state characteristics of the lumped-element inductances at each magnetic node account for the diagonal elements of the tensor permittivity, and the mutual inductances expressed by the arrow symbol account for the off-diagonal elements. The latter characteristics are expressed only at

node  $B$  where the coupling between the electric field components  $E_x$  and  $E_y$  occurs. The gyrator shown in Fig. 5.1(c) is inserted in series with each magnetic node to show the duality of the physical meaning of the circuit variables of both nodes of each transmission line. Figure 5.2 shows the detailed conceptual equivalent circuit at node  $B$ .



$$\begin{pmatrix} \chi_{xx} & \chi_{xy} & 0 \\ \chi_{yx} & \chi_{yy} & 0 \\ 0 & 0 & \chi_{zz} \end{pmatrix} \Longleftrightarrow \begin{pmatrix} \Delta L_x^* & \Delta M_{yx}^* & 0 \\ \Delta M_{xy}^* & \Delta L_y^* & 0 \\ 0 & 0 & \Delta L_z^* \end{pmatrix}$$

(b)

$$\begin{array}{c} \begin{array}{c} I \\ \rightarrow \end{array} \left[ \right] \left[ \begin{array}{c} I^* \\ \rightarrow \end{array} \right] V^* \quad \begin{array}{c} I \\ \rightarrow \end{array} \left[ \right] \left[ \begin{array}{c} I^* \\ \rightarrow \end{array} \right] V^* \\ \\ \begin{pmatrix} V \\ I \end{pmatrix} = \begin{pmatrix} 0 & 1 \\ 1 & 0 \end{pmatrix} \begin{pmatrix} V^* \\ I^* \end{pmatrix} \quad \begin{pmatrix} V \\ I \end{pmatrix} = \begin{pmatrix} 0 & -1 \\ -1 & 0 \end{pmatrix} \begin{pmatrix} V^* \\ I^* \end{pmatrix} \end{array}$$

(c)

Figure 5.1 (a) Conceptual equivalent circuit of magnetized plasma for dc magnetic field  $B_z$ , (b) Correspondence between elements of tensor permittivity and equivalent inductance and (c) Definition of gyrator.

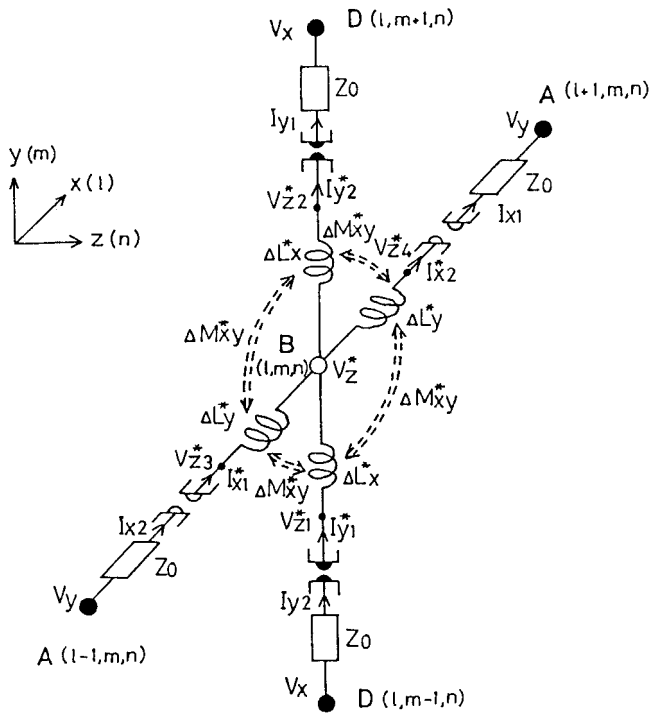


Figure 5.2 Conceptual equivalent circuit at node  $B(l, m, n)$  for DC magnetic field  $B_z$ .

### 5.2 Time-domain Formulation of Magnetized Cold Plasma by Trapezoidal Rule

The equation of motion of particles with electric charge in the magnetized plasma is given by

$$Nm \frac{d\vec{v}}{dt} + Ng\vec{v} = Ne\vec{E} + Ne(\vec{v} \times \vec{B}_0) \quad (53)$$

where  $m$  is the mass of particle,  $g$  is the attenuation constant,  $\vec{E}$  is the electric field,  $N$  is the density of the particles,  $\vec{v}$  is the velocity of particle,  $e$  is the charge of particle, and  $\vec{B}_0$  is the constant magnetic field.

In addition, the electric polarization  $\vec{P}$  is given by

$$\vec{P} = Ne\vec{r} \quad (54)$$

where  $\vec{r}$  is a variable expressing displacement from the equilibrium position of the particle in the plasma. Equation (53) is rewritten using (54) as follows:

$$\frac{d^2\vec{P}}{dt^2} + \frac{g}{m} \frac{d\vec{P}}{dt} - \frac{e}{m} \frac{d\vec{P}}{dt} \times \vec{B}_0 = \frac{Ne^2}{m} \vec{E} \quad (55)$$

In this paper we assume that the constant magnetic field has only a z-directed component (i.e.,  $B_0 = B_z$ ), so we mainly describe the formulation at node  $B$  which is directly concerned with the coupling between field components as described in the previous section. At node  $B$  the electric field components,  $E_x, E_y$ , and magnetic field  $H_z$  are related as shown in Table 2.1. Therefore, the following component equations in (55) are related:

$$\frac{d^2P_x}{dt^2} + \frac{g}{m} \frac{dP_x}{dt} - \frac{eB_0}{m} \frac{dP_y}{dt} = \frac{Ne^2}{m} E_x \quad (56a)$$

$$\frac{d^2P_y}{dt^2} + \frac{g}{m} \frac{dP_y}{dt} + \frac{eB_0}{m} \frac{dP_x}{dt} = \frac{Ne^2}{m} E_y \quad (56b)$$

Also, the following correspondences exist at node  $B$ :

$$V_z^* = H_z \quad I_y^* = -E_x \quad I_x^* = E_y \quad (57a)$$

We then define new equivalent circuit variables  $J_y^*$  and  $J_x^*$  for the polarizations  $P_x$  and  $P_y$ , respectively. The definitions should fundamentally conform to the correspondences of the electric field in (57a), and are given by

$$J_y^* = -P_x \quad J_x^* = P_y \quad (57b)$$



where

$$\omega_\tau : g/m, \quad \omega_c : eB_0/m$$

and

$$\omega_p^2 : Ne^2/\epsilon_0 m \quad (59)$$

Here  $\omega_c$  corresponds to the cyclotron angular frequency and  $\omega_p$  corresponds to the plasma angular frequency. The previous equations are third-order differential equations with respect to time  $t$ , so they may be transformed to finite difference form in the time domain by three-fold application of the trapezoidal rule. The first application of the trapezoidal rule to (58a) and (58b) at time  $t$  yields

$$\begin{aligned} \phi_y''^*(t) = & \epsilon_0 \omega_p^2 (I_y^*(t) - I_y^*(t - \Delta t)) \\ & + \frac{\epsilon_0 \omega_p^2 \omega_\tau \Delta t}{2} (I_y^*(t) + I_y^*(t - \Delta t)) \\ & - \frac{\epsilon_0 \omega_p^2 \omega_c \Delta t}{2} (I_x^*(t) + I_x^*(t - \Delta t)) + \phi_y''^*(t - \Delta t) \end{aligned} \quad (60a)$$

$$\begin{aligned} \phi_x''^*(t) = & \epsilon_0 \omega_p^2 (I_x^*(t) - I_x^*(t - \Delta t)) \\ & + \frac{\epsilon_0 \omega_p^2 \omega_\tau \Delta t}{2} (I_x^*(t) + I_x^*(t - \Delta t)) \\ & + \frac{\epsilon_0 \omega_p^2 \omega_c \Delta t}{2} (I_y^*(t) + I_y^*(t - \Delta t)) + \phi_x''^*(t - \Delta t) \end{aligned} \quad (60b)$$

where

$$\phi_y''^*(t) = \frac{d^2 J_y^*(t)}{dt^2} + 2\omega_\tau \frac{dJ_y^*(t)}{dt} + (\omega_c^2 + \omega_\tau^2) J_x^*(t) \quad (61a)$$

$$\phi_x''^*(t) = \frac{d^2 J_x^*(t)}{dt^2} + 2\omega_\tau \frac{dJ_x^*(t)}{dt} + (\omega_c^2 + \omega_\tau^2) J_y^*(t) \quad (61b)$$

and  $\Delta t$  is the time increment. The second application of the trapezoidal rule to (60a) and (60b) at  $t$ , using (60a) and (60b) at  $t - \Delta t$ , yields

$$\begin{aligned} \phi_y'^*(t) = & \frac{\epsilon_0 \omega_p^2 \Delta t}{2} (I_y^*(t) - I_y^*(t - \Delta t)) \\ & + \frac{\epsilon_0 \omega_p^2 \omega_\tau \Delta t^2}{4} (I_y^*(t) + I_y^*(t - \Delta t)) \\ & - \frac{\epsilon_0 \omega_p^2 \omega_c \Delta t^2}{4} (I_x^*(t) + I_x^*(t - \Delta t)) \\ & + \Delta t \phi_y''^*(t - \Delta t) + \phi_y'^*(t - \Delta t) \\ & + (\omega_c^2 + \omega_\tau^2) \Delta t J_y^*(t - \Delta t) \end{aligned} \quad (62a)$$

$$\begin{aligned}
\phi_x'^*(t) = & \frac{\epsilon_0 \omega_p^2 \Delta t}{2} (I_x^*(t) - I_x^*(t - \Delta t)) \\
& + \frac{\epsilon_0 \omega_p^2 \omega_\tau \Delta t^2}{4} (I_x^*(t) + I_x^*(t - \Delta t)) \\
& + \frac{\epsilon_0 \omega_p^2 \omega_c \Delta t^2}{2} (I_y^*(t) + I_y^*(t - \Delta t)) \\
& + \Delta t \phi_x''^*(t - \Delta t) + \phi_x'^*(t - \Delta t) \\
& + (\omega_c^2 + \omega_\tau^2) \Delta t J_x^*(t - \Delta t)
\end{aligned} \tag{62b}$$

where

$$\phi_y'^*(t) = \frac{dJ_y^*(t)}{dt} + \left( 2\omega_\tau + \frac{\omega_\tau^2 \Delta t}{2} + \frac{\omega_c^2 \Delta t}{2} \right) J_y^*(t) \tag{63a}$$

$$\phi_x'^*(t) = \frac{dJ_x^*(t)}{dt} + \left( 2\omega_\tau + \frac{\omega_\tau^2 \Delta t}{2} + \frac{\omega_c^2 \Delta t}{2} \right) J_x^*(t). \tag{63b}$$

Next, the relation between the time variations of electric polarization and the magnetic field are formulated as follows. For the equivalent inductance at a magnetic node, the time derivative of the electric flux  $J_y^*$ ,  $J_x^*$  causes a variation of the voltage drop  $V_y^*$ ,  $V_x^*$  through each inductance that corresponds to the variation of the magnetic field.

$$V_y^*(t) = \Delta d \frac{dJ_y^*(t)}{dt} \tag{64a}$$

$$V_x^*(t) = \Delta d \frac{dJ_x^*(t)}{dt}. \tag{64b}$$

Equation (64a) and (64b) are also transformed to finite difference form by using the trapezoidal rule:

$$J_y^*(t) = \frac{\Delta t}{2\Delta d} (V_y^*(t) + V_y^*(t - \Delta t)) + J_y^*(t - \Delta t) \tag{65a}$$

$$J_x^*(t) = \frac{\Delta t}{2\Delta d} (V_x^*(t) + V_x^*(t - \Delta t)) + J_x^*(t - \Delta t) \tag{65b}$$

After the third application of the trapezoidal rule to (61a) and (61b), and substituting (65a) and (65b) into the resultant equations, we finally obtain the difference equations in the time domain for the magnetized plasma as follows:

$$\begin{aligned}
V_y^*(t) - R_L I_y^*(t) + R_M I_x^*(t) = & -V_y^*(t - \Delta t) - R_L I_y^*(t - \Delta t) \\
& - R_M I_x^*(t - \Delta t) - K_1 J_y^*(t - \Delta t) \\
& + K_2 \phi_y'^*(t - \Delta t) + K_3 \phi_y''^*(t - \Delta t)
\end{aligned} \tag{66a}$$

$$\begin{aligned}
V_x^*(t) - R_L I_x^*(t) - R_M I_y^*(t) = & -V_x^*(t - \Delta t) - R_L I_x^*(t - \Delta t) \\
& + R_M I_y^*(t - \Delta t) - K_1 J_x^*(t - \Delta t) \\
& + K_2 \phi_x'^*(t - \Delta t) + K_3 \phi_x''^*(t - \Delta t)
\end{aligned} \tag{66b}$$

where

$$R_L = (1 + \omega_\tau \Delta t / 2) \epsilon_0 \omega_p^2 \Delta t^2 / 4A \tag{66c}$$

$$R_M = \epsilon_0 \omega_c \omega_p^2 \Delta t^3 / 8A \tag{66d}$$

$$K_1 = 2\Delta t (\omega_\tau (1 + \omega_\tau \Delta t / 2) + \omega_c^2 \Delta t / 2) / A \tag{66e}$$

$$K_2 = \Delta t / A \tag{66f}$$

$$K_3 = \Delta t^2 / 2A \tag{66g}$$

$$A = ((1 + \omega_\tau \Delta t / 2)^2 + (\omega_c \Delta t / 2)^2) \Delta t / 2\Delta d. \tag{66h}$$

The quantities  $\phi'^*$  and  $\phi''^*$  correspond to the first and the second derivatives of the flux  $J^*$  in successive time steps, respectively. Thus the third-order difference equations are transformed into iterative difference equations in the time domain involving only variables obtained at the previous time step.  $R_L^*$  and  $R_M^*$  correspond to the time-domain characteristic admittance of the self-inductance and mutual inductance shown in Fig. 5.2. As shown in Fig. 5.3, the foregoing difference equations represent an equivalent circuit with dependent sources for the time-domain self- and mutual inductances in each line, where each  $E_i$  ( $i=1,4$ ) for the current sources corresponds to the right sides of (66a) and (66b), respectively. The difference in the polarity of the dependent voltage sources  $R_M^* I_x^*$  and  $R_M^* I_y^*$  expresses the anisotropy of the magnetized plasma.

### 5.3 Bergeron's Formulation

In previous section, the derivation of the time-domain finite-difference equations of the magnetized plasma is explained. In this section we combine these equations with the Bergeron formulation of wave propagation and formulate the nodal equation at node  $B$ . As shown in Fig. 5.2, by considering the voltage variables  $V_{z1}^*(l, m, n, t)$ ,  $V_{z2}^*(l, m, n, t)$ ,  $V_{z3}^*(l, m, n, t)$ , and  $V_{z4}^*(l, m, n, t)$  in each line, the voltage drops at the inductances for (65a) and (65b) are given by

$$V_{y1}^*(l, m, n, t) = V_{z1}^*(l, m, n, t) - V_z^*(l, m, n, t) \tag{67a}$$



$$V_{y2}^*(l, m, n, t) = V_z^*(l, m, n, t) - V_{z2}^*(l, m, n, t) \quad (67b)$$

$$V_{x1}^*(l, m, n, t) = V_{z3}^*(l, m, n, t) - V_z^*(l, m, n, t) \quad (67c)$$

$$V_{x2}^*(l, m, n, t) = V_z^*(l, m, n, t) - V_{z4}^*(l, m, n, t) \quad (67d)$$

where  $V_z^*(l, m, n, t)$  is the voltage at the node point  $B(l, m, n)$ , and the parameters  $l$ ,  $m$ ,  $n$  and  $t$  denote the discretized position numbers of the  $x$ ,  $y$ , and  $z$  directions and time, respectively.

On the other hand, the Bergeron expression for each transmission line at node  $B(l, m, n)$  is given by

$$\begin{aligned} V_{z1}^*(l, m, n, t) + z_0^* I_{y1}^*(l, m, n, t) = \\ - (I_{y2}(l, m - 1, n, t - \Delta t) + z_0^* V_x(l, m - 1, n, t - \Delta t)) \end{aligned} \quad (68a)$$

$$\begin{aligned} V_{z2}^*(l, m, n, t) - z_0^* I_{y2}^*(l, m, n, t) = \\ - (I_{y1}(l, m + 1, n, t - \Delta t) - z_0^* V_x(l, m + 1, n, t - \Delta t)) \end{aligned} \quad (68b)$$

$$\begin{aligned} V_{z3}^*(l, m, n, t) + z_0^* I_{x1}^*(l, m, n, t) = \\ I_{x2}(l - 1, m, n, t - \Delta t) + z_0^* V_y(l - 1, m, n, t - \Delta t) \end{aligned} \quad (68c)$$

$$\begin{aligned} V_{z4}^*(l, m, n, t) - z_0^* I_{x2}^*(l, m, n, t) = \\ I_{x1}(l + 1, m, n, t - \Delta t) - z_0^* V_y(l + 1, m, n, t - \Delta t) \end{aligned} \quad (68d)$$

where  $\Delta t$  is the time step which corresponds to the propagation time in each transmission line and, in this formulation, also coincides with the time step in the difference equations for the magnetized plasma. The quantity  $z_0^*$  is the characteristic admittance of the line. Substituting (68a)(68d) and (67a)(67d) into (66a) and (66b) and considering the correspondence to each line results in

$$\begin{aligned} V_z^*(l, m, n, t) + (z_0^* + R_L^*) I_{y1}^*(l, m, n, t) = \\ A_1 - E_1 + R_M^* I_x^*(l, m, n, t) \end{aligned} \quad (69a)$$

$$\begin{aligned} V_z^*(l, m, n, t) - (z_0^* + R_L^*) I_{y2}^*(l, m, n, t) = \\ A_2 + E_2 - R_M^* I_x^*(l, m, n, t) \end{aligned} \quad (69b)$$

$$\begin{aligned} V_z^*(l, m, n, t) + (z_0^* + R_L^*) I_{x1}^*(l, m, n, t) = \\ A_3 - E_3 - R_M^* I_y^*(l, m, n, t) \end{aligned} \quad (69c)$$

$$\begin{aligned} V_z^*(l, m, n, t) - (z_0^* + R_L^*) I_{x2}^*(l, m, n, t) = \\ A_4 + E_4 + R_M^* I_y^*(l, m, n, t) \end{aligned} \quad (69d)$$

where  $E_1$ ,  $E_2$ ,  $E_3$ , and  $E_4$  correspond to the right sides of (66a) and (66b), and  $A_1$ ,  $A_2$ ,  $A_3$ , and  $A_4$  correspond to the right sides of (68a)–(68d), respectively. These equations are evaluated using only values computed at the procedure. We define each coupling term  $I_x^*$ ,  $I_y^*$  on the right sides of (69a)–(69d) as follows:

$$I_x^*(l, m, n, t) = I_{x1}^*(l, m, n, t) + I_{x2}^*(l, m, n, t) \quad (70a)$$

$$I_y^*(l, m, n, t) = I_{y1}^*(l, m, n, t) + I_{y2}^*(l, m, n, t) \quad (70b)$$

and these are obtained as follows from (69a)–(69d):

$$I_x^*(l, m, n, t) = \frac{(A_1 - A_2 - E_1 - E_2)(z_0^* + R_L^*) + 2(A_3 - A_4 - E_3 - E_4)R_M^*}{(z_0^* + R_L^*)^2 + 4R_M^{*2}} \quad (71a)$$

$$I_y^*(l, m, n, t) = \frac{(A_3 - A_4 - E_3 - E_4)(z_0^* + R_L^*) - 2(A_1 - A_2 - E_1 - E_2)R_M^*}{(z_0^* + R_L^*)^2 + 4R_M^{*2}} \quad (71b)$$

From (69a)–(69d), (71a), (71b), and the continuity of the current at node  $B(l, m, n)$ , the unified nodal equation at the time  $t$  is given by

$$V_z^*(l, m, n, t) = \frac{F_1^* + F_2^* + F_3^* + F_4^*}{4} \quad (72)$$

where,  $F_1^*$ ,  $F_2^*$ ,  $F_3^*$ , and  $F_4^*$  correspond to the right sides of (69a)–(69d), respectively. Each current component at time  $t$  is calculated by using  $V_z^*(l, m, n, t)$  as follows:

$$I_{y1}^*(l, m, n, t) = (F_1^* - V_z^*(l, m, n, t)) / (z_0^* + R_L^*) \quad (73a)$$

$$I_{y2}^*(l, m, n, t) = -(F_2^* - V_z^*(l, m, n, t)) / (z_0^* + R_L^*) \quad (73b)$$

$$I_{x1}^*(l, m, n, t) = (F_3^* - V_z^*(l, m, n, t)) / (z_0^* + R_L^*) \quad (73c)$$

$$I_{x2}^*(l, m, n, t) = -(F_4^* - V_z^*(l, m, n, t)) / (z_0^* + R_L^*) \quad (73d)$$

The quantities  $V_{z1}^* - V_{z4}^*$ ,  $J_{x1}^*$ ,  $J_{x2}^*$ ,  $J_{y1}^*$ ,  $J_{y2}^*$ ,  $\phi'_{x1}$ ,  $\phi'_{x2}$ ,  $\phi'_{y1}$ ,  $\phi'_{y2}$ ,  $\phi''_{x1}$ ,  $\phi''_{x2}$ ,  $\phi''_{y1}$  and  $\phi''_{y2}$  are similarly evaluated. At nodes  $C$  and  $F$  the resultant formulations correspond formally to the previous equations with the mutual coupling terms removed. The time response of the field in the overall region is computed by iteration in the time

domain. In this analysis, the direction of the constant magnetic field is supposed to the  $z$  direction. However, should the constant magnetic field have another direction, the corresponding equivalent circuit may be similarly derived.

#### 5.4 Numerical Results and Discussion

To examine the validity of the formulation described in the preceding section, we at first simulate the extraordinary mode propagation of a plane wave for the transversely magnetized condition. To simulate such propagation of the extraordinary wave in the  $xy$  plane, the model shown in Fig. 5.4 is used. The distance between the top and bottom magnetic walls is very small and the width is sufficient that the influence of the sides is neglected near the center. The boundary condition for the magnetic walls is that  $H_x$ ,  $H_y$ , and  $E_z$  are zero. These conditions indicate that only the field components  $E_x$ ,  $E_y$ , and  $H_z$  exist. A sinusoidal wave of  $H_z$  is applied to the input plane. The free-space wavelength of the input wave  $\lambda_0$  is  $25\Delta d$ . The output plane and side planes are approximated as reflectionless boundaries by the use of the matching impedance. In this analysis,  $\omega_\tau$  is assumed to be zero. Figures 5.5-5.7 show the computed and analytic wavelengths in the steady state as functions of the parameters  $\omega_p$  and  $\omega_c$ . The analytical wavelength  $\lambda$  in the steady state is given by

$$\lambda = \lambda_0 / \sqrt{(\epsilon_{xx} - \epsilon_{xy}^2 / \epsilon_{xx})} \quad (74a)$$

where

$$\epsilon_{xx} = 1 + \omega_p^2 / (\omega_c^2 - \omega^2) \quad (74b)$$

$$\epsilon_{xy} = \omega_p^2 \omega_c / \omega (\omega_c^2 - \omega^2) \quad (74c)$$

and  $\omega$  is the angular frequency of the input wave. In these figures the values of computed wavelength agree well with the corresponding analytical ones in every case. Therefore, the validity of the formulation is verified for this transversely magnetized condition.

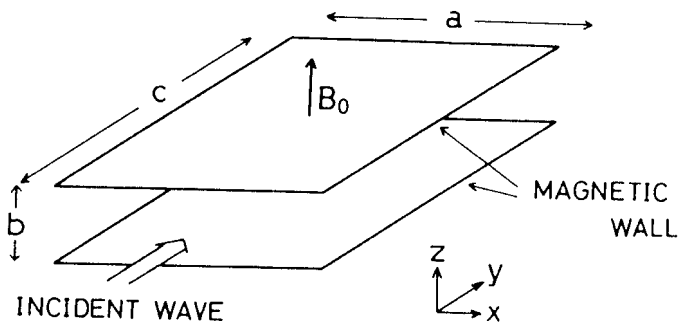


Figure 5.4 Analyzed model of parallel magnetic-wall waveguide ( $a = 180\Delta d$ ,  $b = 2\Delta d$  and  $c = 300\Delta d$ .)

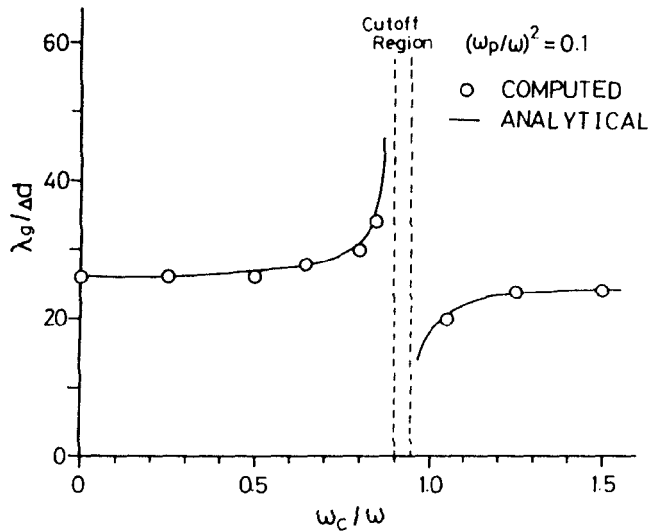


Figure 5.5 Computed wavelength versus analytical one ( $(\omega_p/\omega)^2 = 0.1$ ,  $\omega_\tau = 0.0$ ).

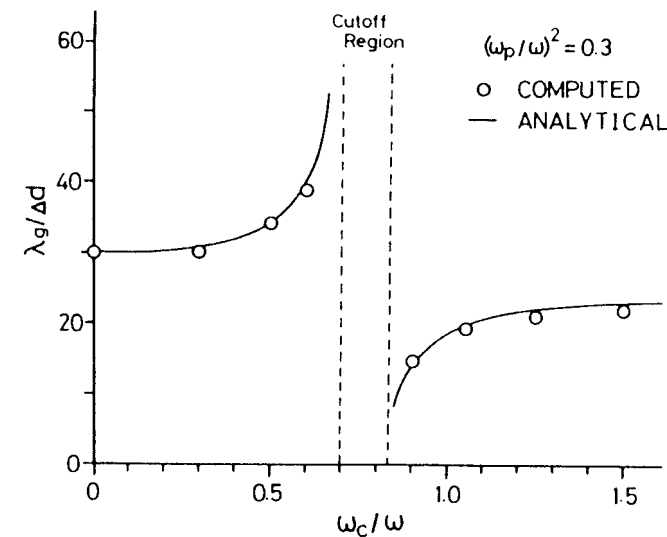


Figure 5.6 Computed wavelength versus analytical one ( $(\omega_p/\omega)^2 = 0.3$ ,  $\omega_\tau = 0.0$ )

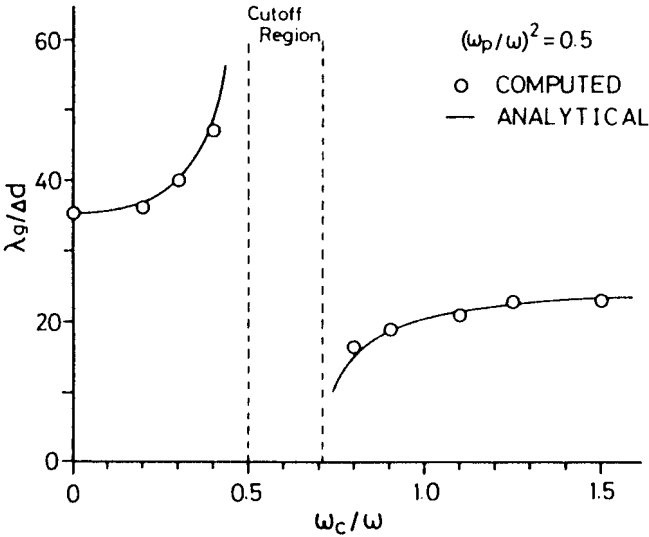
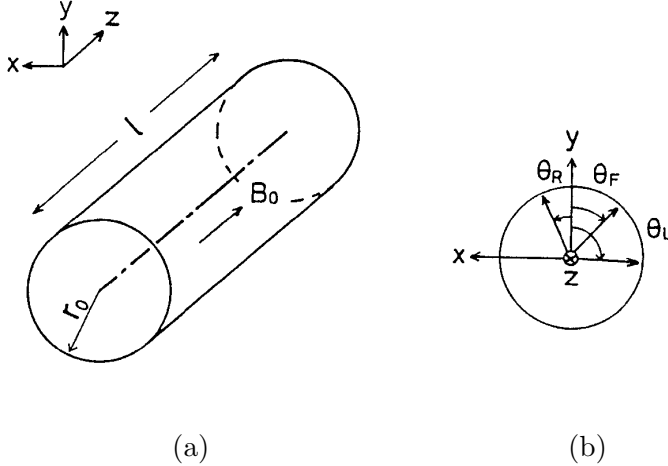


Figure 5.7 Computed wavelength versus analytical one ( $(\omega_p/\omega)^2 = 0.5$ ,  $\omega_\tau = 0.0$ )

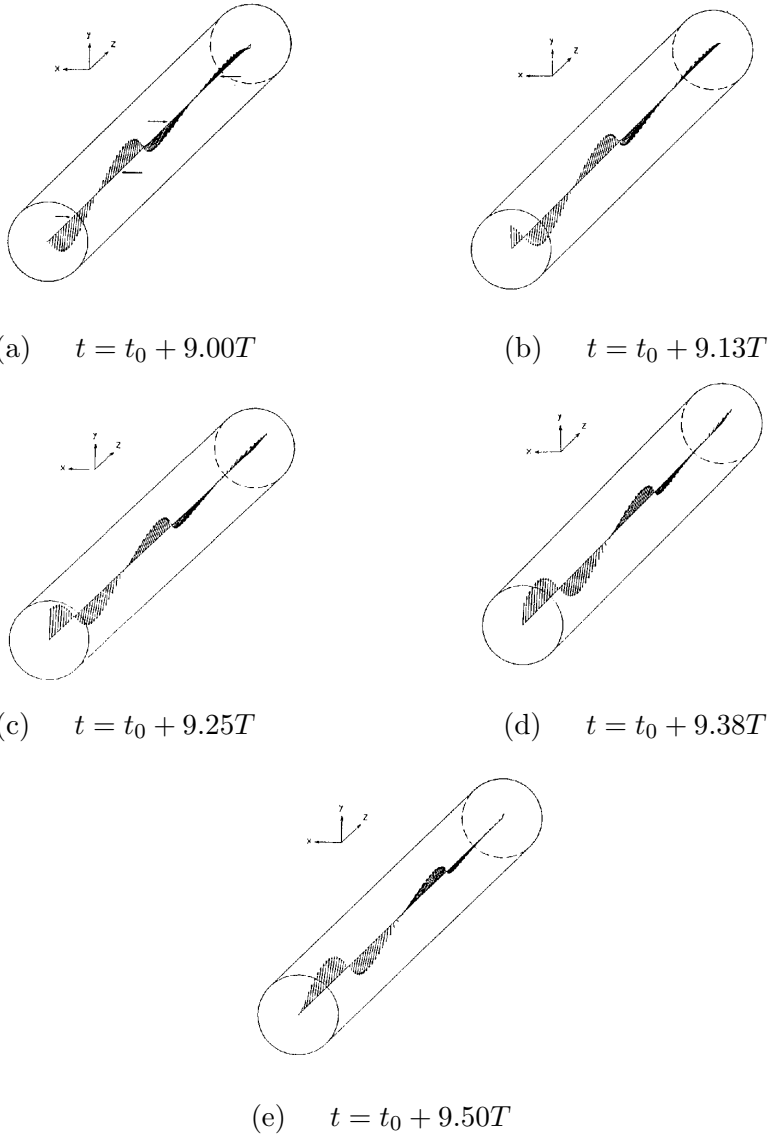
Next we simulated Faraday rotation in a longitudinally magnetized cylindrical waveguide. Figure 5.8(a) shows the model of the cylindrical waveguide, and Fig. 5.8(b) shows the coordinate system for the angles of the planes of polarization  $\theta_L$ ,  $\theta_R$  and  $\theta_F$ .  $\theta_L$ ,  $\theta_R$ , and  $\theta_F$  are the rotation angles along the  $z$  direction for the L-wave, the R-wave, and the linear polarization, respectively. The wall of the cylindrical waveguide is approximated by stairs because of the cubic lattice network of the present method. The boundary condition on the wall of the waveguide is assumed to correspond to perfect conductivity. The sinu-soidal wave is applied in the input plane. The mode of the input wave is supposed to be the  $TE_{11}$  mode. The output plane is terminated by the characteristic impedance of the  $TE_{11}$  mode to approximate the matching condition. The frequency  $f = 1.28f_{cn}$ , where  $f_{cn}$  is the cut-off frequency for the  $TE_{11}$  mode. The parameters of the plasma are given by  $(\omega_p/\omega) = 0.1$ ,  $\omega_c/\omega = 0.5$ , and  $\omega_\tau = 0$ , where  $\omega$  is the angular frequency of the input wave. In the following figures  $t$  is the observation time and  $T$  denotes the period of the applied wave. The input is applied at  $t = 0$ .



**Figure 5.8** (a) Analyzed model of plasma-filled cylindrical waveguide ( $r_0 = 15\Delta d$ ,  $l = 150\Delta d$ ), (b) Coordinate system of angle of rotation  $\theta_L$  for L-wave,  $\theta_R$  for R-wave,  $\theta_F$  for linear polarization.

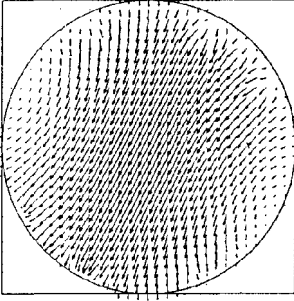
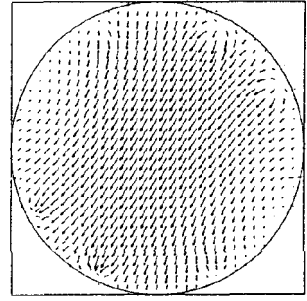
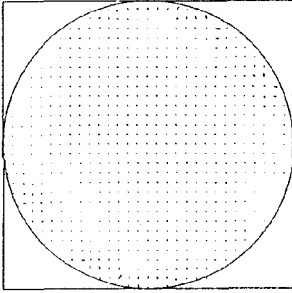
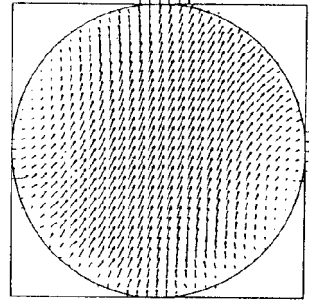
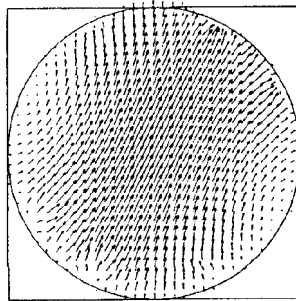
Figure 5.9 shows the time variation of the rotation of the electric field for a half-period along the central axis for linearly polarized input. The electric field rotates in the right hand sense with increasing  $z$ . This phenomenon is supposed to be Faraday rotation. Figure 5.10 shows the time variation of the instantaneous pattern of the electric field in the cross section at  $z = 90\Delta d$ . In these figures the rotation of the  $TE_{11}$  mode is shown. Theoretically, under these conditions the refractive index for the R-wave is smaller than that of the L-wave, so the phase velocity of the R-wave is larger than that of the L-wave. Therefore,  $\theta_F$  should rotate to the left as  $z$  increases. On the other hand, at each position on the  $z$  axis the previous condition results in elliptical polarization that rotates to the right. Figures 5.9 and 5.10 corroborate this.

Finally, to validate the existence of the Faraday rotation, we verify that the composition of the R-wave and the L-wave of circular polarization causes the rotation of the linear polarization. Figure 5.11 shows the variation of the angles and  $\theta_R$  of  $\theta_L$  the electric fields of the R-wave and the L-wave versus the propagation distance along the  $z$  axis at  $t = 9.0T$  as shown in Fig. 5.9(a), respectively. The  $\theta_F$  are also plotted, having been obtained from the angle of the points of maximum amplitude of the electric field as indicated in Fig. 5.9(a) by arrows.  $\theta_L$  and  $\theta_R$  thus obtained are proportional to the propagation distance. The inclination of  $\theta_L$  is greater than that of  $\theta_R$ , so the phase velocity of the R-wave larger than that of the L-wave. This shows that the propagation characteristics of the R- and L-waves are well simulated. Comparing a plot of  $(\theta_L - \theta_R)/2$  with plotted values of  $\theta_F$  also shows close agreement. Theoretically, for Faraday rotation the points of maximum amplitude occur when the condition  $(\theta_L + \theta_R)/2 = 180n$  (where  $n$  is an integer) is satisfied. In Fig. 5.11, this phenomenon is observed for each of the points corresponding to plotted values of  $\theta_F$ .

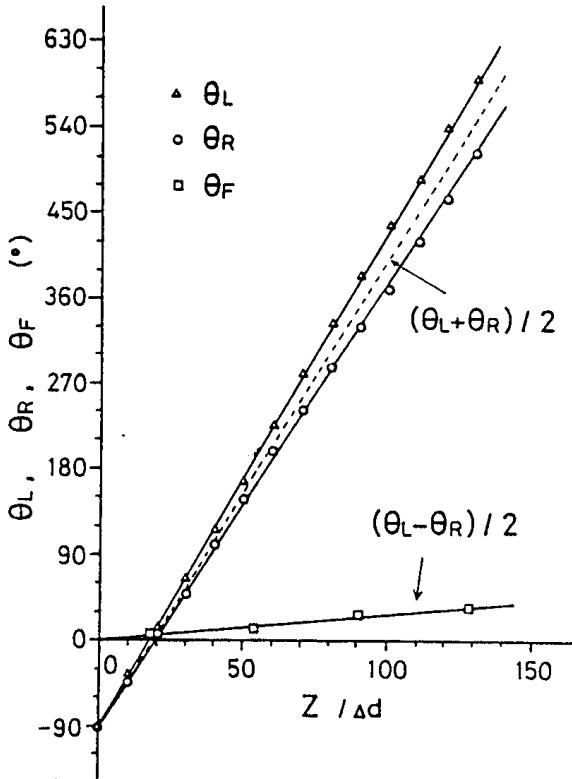


**Figure 5.9** Time variation of electric field distribution on central axis of waveguide ( $(\omega_P/\omega)^2 = 0.1$ ,  $\omega_c/\omega = 0.5$  and  $\omega_\tau = 0.0$ )



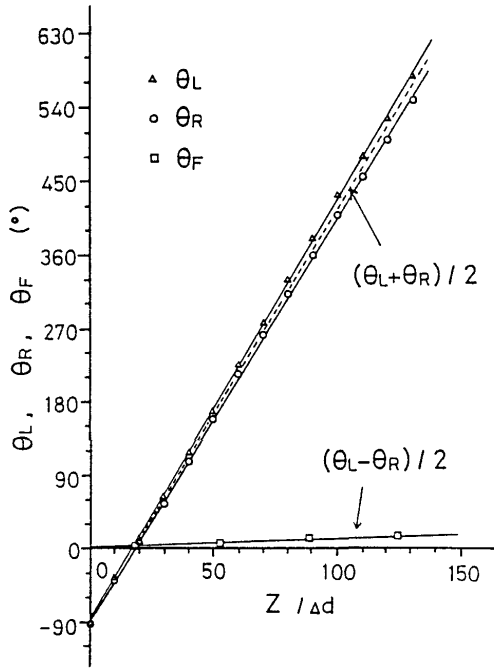

 (a)  $t = t_0 + 9.00T$ 

 (b)  $t = t_0 + 9.13T$ 

 (c)  $t = t_0 + 9.25T$ 

 (d)  $t = t_0 + 9.38T$ 

 (e)  $t = t_0 + 9.50T$ 

**Figure 5.10** Time variation of electric field distribution on cross section  $((\omega_P/\omega)^2 = 0.1, \omega_c/\omega = 0.5, \omega_\tau = 0.0$  and  $z = 90\Delta d$ ).



**Figure 5.11** Angles of rotation  $\theta_R$ ,  $\theta_L$ , and  $\theta_F$  versus propagation distance ( $(\omega_P/\omega)^2 = 0.1$ ,  $\omega_c/\omega = 0.5$ ,  $\omega_\tau = 0.0$  and  $t = 9.0T$ )

Similarly, Fig. 5.12 shows the angles of rotation  $\theta_r$ ,  $\theta_L$ , and  $\theta_F$  versus the propagation distance for  $\omega_c/\omega = 0.25$  under the same conditions as in Fig. 5.11, and the results are similar. The angle  $\theta_F$  should be proportional to  $\omega_c$  and  $\theta_F$  in Fig. 5.12 is half of that in Fig. 5.11 as expected. From these considerations we conclude that Faraday rotation is validly reflected in this formulation.



**Figure 5.12** Angles of rotation  $\theta_R$ ,  $\theta_L$ , and  $\theta_F$  versus propagation distance ( $(\omega_P/\omega)^2 = 0.1$ ,  $\omega_c/\omega = 0.25$ ,  $\omega_\tau = 0.0$  and  $t = 9.0T$ ).

## 6. Conclusion

In this paper we developed the fundamental treatment of the anisotropic medium in the Spatial Network Method for a three-dimensional analysis in the time domain. As examples, the formulation of the uniaxial anisotropy of dielectric medium and the gyroanisotropy such as the magnetized ferrite and the magnetized plasma were presented.

The iterative procedure very closely matches the architecture for high speed computation in the vector processor of a super computer. This property can render practical the simulation of three-dimensional fields involving anisotropic medium and expand the generality of the numerical vector analysis method in the time domain.

In these analysis presented in this paper, we treat the case of a specific direction of the constant magnetic field, but the formulation for arbitrary direction can be performed in the same way. We are applying these is treatment to many kinds of nonreciprocal devices involving complicated boundary conditions, and studying transient properties for the high speed pulse waves in the MIC. These results will be reported in later papers [24–26].

## References

1. Kron, G., "Equivalent circuit of the field equations of Maxwell-I," *Proc. IRE*, Vol. 32, 289–299, 1944.
2. Tumolillo, T. A., and J. P. Wondra, "MEEC-3D:A computer code for self-consistent solution of the Maxwell-Lorentz equations in three dimensions," *IEEE Trans. Nuclear Science*, Vol. NS-24, 2449–2455, 1977.
3. Yee, K. S., "Numerical solution of initial boundary value problems involving Maxwell's equations in isotropic media," *IEEE Trans. Antennas and Propagation*, Vol. AP-14, 302–307, 1966.
4. Taflove, A., and M. E. Brodwin, "Numerical solution of steady-state electromagnetic scattering problems using the time-dependent Maxwell's equations," *IEEE Trans. Microwave Theory and Techniques*, Vol. MTT-23, 623–630, 1975.
5. Holland, R., "THREDE: A Free-field EMP coupling and scattering code," *IEEE Trans. Nuclear Science*, Vol. NS-24, 2416–2421, 1977.
6. Johns, P. B., and R. L. Beurle, "Numerical solution of two-dimensional scattering problems using a transmission line matrix," *Proc. IEE*, Vol. 118, 1203–1205, 1971.
7. Akhtarzad, S., and P. B. Johns, "Solution of Maxwell's equations in three space dimensions and time by the t.l.m method of numerical analysis," *Proc. IEE*, Vol. 122, 1344–1348, 1975.
8. Hoefer, W. J. R., "The transmission-line matrix method—Theory and Applications," *IEEE Trans. Microwave Theory and Techniques*, Vol. MTT-33, 882–893, 1985.
9. Mariki, G. E., and C. Yeh, "Dynamic three-dimensional TLM analysis of microstriplines on anisotropic substrate," *IEEE Trans. Microwave Theory and Techniques*, Vol. MTT-33, 789–799, 1985.

10. Alexopoulos, N. G., "Integrated-circuit structures on anisotropic substrates," *IEEE Trans. Microwave Theory and Techniques*, Vol. MTT-33, 847–881, 1985.
11. Yoshida, N., I. Fukai, and J. Fukuoka, "Transient analysis of two-dimensional Maxwell's equations by Bergeron's method," *Trans. IECE Japan(B)*, Vol. J62-B, 511–518, 1979.
12. Yoshida, N., I. Fukai, and J. Fukuoka, "Transient analysis of three-dimensional electromagnetic fields by nodal equations," *Trans. IECE Japan(B)*, Vol. J63-B, 876–883, 1980.
13. Yoshida, N., I. Fukai, and J. Fukuoka, "Adaptation of Bergeron's method to complicated boundary problems," *Trans. IECE Japan(E)*, Vol. E64, 455–462, 1981.
14. Yoshida, N., and I. Fukai, "Transient analysis of a stripline having a corner in three-dimensional space," *IEEE Trans. Microwave Theory and Techniques*, Vol. MTT-32, 491–498, 1984.
15. Bergeron, L. J. B., *Du Coup de Belier en Hydraulique au Coup de Founder en electricite*, Dunod, Paris, 1949.
16. Dommel, H. W., "Digital computer solution of electromagnetic transients in single- and multiphase network," *IEEE Trans. Power Apparatus and Systems*, Vol. PAS-88, 388–396, 1969.
17. Metzger, G., and J-P. Pabre, *Transmission Lines with Pulse Excitation*, Academic Press, New York, 1969.
18. Yoshida, N., I. Fukai, and J. Fukuoka, "Application of Bergeron's method to anisotropic media," *Trans. IECE Japan(B)*, Vol. J64-B, 1242–1249, 1981.
19. Koike, S., N. Yoshida, and I. Fukai, "Transient analysis of microstrip line on anisotropic substrate in three-dimensional space," *IEEE Trans. Microwave Theory and Techniques*, Vol. MTT-36, 34–43, 1988.
20. Kukutsu, N., N. Yoshida, and I. Fukai, "Transient analysis of ferrite in three-dimensional space," *IEEE Trans. Microwave Theory and Techniques*, Vol. MTT-36, 114–125, 1988.
21. Kashiwa, T., N. Yoshida, and I. Fukai, "Transient analysis of a magnetized plasma in three-dimensional space," *IEEE Trans. Antennas and Propagation*, Vol. 36, 1096–1105, 1988.
22. Bhat, B., and S. K. Koul, "New approach to strip- and microstrip-like transmission lines with anisotropic substrate having a tilted optical axis," *Proc. IEE*, Vol. 131, pt. H, 191–197, 1984.

23. Waldron, R. A., "Electromagnetic wave propagation in cylindrical waveguide containing gyromagnetic media," *J. Brit. Inst. Radio Eng.*, 597–612, 6; 7–690, and 733–746, 1958.
24. Ko, Y., N. Yoshida, and I. Fukai, "Three-dimensional electromagnetic analysis of rectangular waveguide containing high-permittivity anisotropic dielectric," *Electronics and Communications in Japan*, Part 2, Vol. 74, 1–6, 1991.
25. Kukutsu, N., N. Yoshida, and I. Fukai, "Transient analysis of a junction circulator for microstrip line in three-dimensional space," *Trans. IEICE in Japan(C)*, Vol. J71-C, 894–905, 1988.
26. Kashiwa, T., N. Yoshida, and I. Fukai, "Time domain analysis of patch antennas in a magnetized plasma by the spatial network method," *IEEE Trans. Antennas and Propagation*, Vol. 39, 147–150, 1991.